LABORATOIRE MATÉRIAUX ET PHÉNOMÈNES QUANTIQUES

UNIVERSITÉ PARIS CITÉ

MASTER 2 QUANTUM DEVICES

MASTER's degree in NANOTECHNOLOGIES FOR ICTs

Internship Report

MAGNETIC DAMPING AND SPIN PUMPING AT COBALT-BIDIMENSIONAL MATERIALS INTERFACES

Supervisors	Candidate
FRANÇOIS MALLET	**ROBERTO BELLELLI**
CLÉMENT BARRAUD	

Paris, June 2024

Summary

The report describes the four months work done in the TELEM research group. This experimental internship covers all the activities required for experimental research in mesoscopic physics, starting from devices design, fabrication and characterization, to data acquisition and analysis; moreover, the project deepens the concepts and the notions of condensed matter physics at the nanoscale. Therefore here I will briefly present the physical theories behind the materials and the models provided by quantum mechanics, along with the equations that rule the physics and the working principles of the devices.

The work mainly focuses on the realization of bidimensional heterostructures; the device under test is realized by using different nanofabrication techniques and it is devoted to spintronics applications i.e. aims to benefit from the manipulation of the electron's degree of freedom called *spin*. I will rather make the focus here that spintronics has reached several important successes with bulk materials but to go further, the idea to exploit bidimensional materials- either in monolayers or in heterostructures- as a platform for spin injection, propagation and detection is very exciting, due to the great tunability and versatility they offer.

In particular, in this study the modulation by proximity effects of two-dimensional materials -such as graphene and transition-metal dichalcogenides- of the dissipation of the *ferromagnetic resonance* is explored for cobalt: the goal of the project is the generation and the detection through *spin pumping* of pure spin currents in 2D materials and its independent detection through *inverse spin Hall effect*.

Table of Contents

1. Introduction

1.1 Team and laboratory

The stage is carried out with the Transport Électronique à L'Échelle Moléculaire (TELEM) team, which works at Laboratoire Matériaux et Phénomènes Quantiques (MPQ), a research unit of the Center National de la Recherche Scientifique (CNRS) and Université Paris Cité. In the TELEM team innovative methods and fabrication techniques, new experimental setups and different approaches lead to study charge, spin, and heat transfer in two-dimensional (2D) materials. The team who follows me is mainly composed by the supervisors François Mallet and Clément Barraud, and the PhD student Karen Sobnath, whose work guided me during the time spent in the team. Their work is focused on the study of devices devoted to spintronics: spintronics is the field of electronics which aims to take benefits not only from the charge but also from the spin and which had many successes in the recent years. Particularly interesting is the focusing on 2D materials and the possibility to combine them to exploit new properties and quantum effects: therefore, among the most famous examples of 2D materials that I exploit during my work we have graphene, transition-metal-dichalcogenides and hexagonal boron nitride.

The fabrication processes and characterization experiments are mainly performed in two fundamental laboratory units: the TELEM laboratory, equipped with a Radio-Frequency (RF) experimental platform for ultra-low-noise measurements and magnetotransport experiments, developed at room temperature and capable to reach 0.5 Tesla of magnetic field (while they are currently developing a new platform with 7 Tesla at 1.5 kelvin); the cleanroom (salle blanche), an environment where particulate concentration is reduced and kept under a specified level as well as controlled temperature and humidity. The majority of the fabrication procedures are exploited in this kind of environment since the scale of precision of the work is micro-nano-metric, and even the smallest contamination can ruin the devices and lead the chips to fail, poison the equipment and pose a serious and non negligible health risk.

1.2 Spintronics and 2D materials

Spintronics has rapidly gained interest in recent decades due to its promising ability to revolutionize the technological landscape. In contrast to conventional electronics, which is based on the transport of electric charges, spintronics exploits the quantum property of electrons called *spin* -i.e. the electron intrinsic angular momentum- and the correspondent magnetic moment for the storage and transfer of information. Electronics controls the charge transport by applying either a voltage or an electric field and the detection is mostly based on current-voltage reading e.g. using transistors; conversely, in spintronics, spin is usually controlled by magnetic field and electrical currents (since moving electrons carry both charge and spin). Indeed in spintronics one of the most important concepts is represented by the spin-polarized current: it is a flow of electric charge carriers, such as electrons, in which the majority of the carriers have their spins aligned in a particular direction. In other words, the current consists predominantly of electrons with their spins pointing either up or down, rather than an equal mixture of both. A fully spin-polarized current would consist entirely of charge carriers with spins aligned in the same direction, while a partially spin-polarized current would have a majority of carriers with aligned spins but some fraction with spins in the opposite direction. The concept of spin-polarized currents is crucial in spintronics because it allows for the manipulation and detection of spin information. However let us do a step further and introduce the concept of pure spin current i.e. flow of spin without the accompanying flow of electric charge. In other words, it consists of a net transfer of spin information through a material, with no net movement of charge carriers. Pure spin currents are of particular interest in spintronics because they enable the manipulation and transport of spin information without the need for charge transport, which can lead to more efficient and less dissipating and versatile devices. A comparison between these kind of currents is proposed in Fig. 1.1.

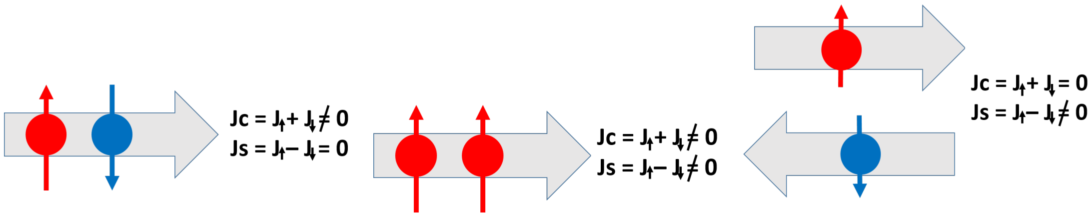

(a) (b) (c)

Figure 1.1: Definition of: charge current **(a)**, flow of electric charge (conventional current), where electron spins are typically random; spin polarized current **(b)**, flow of electric charge with an unbalance in electron spins (net spin polarization); pure spin current **(c)**, flow of spin angular momentum without a net flow of electric charge.

Some important basic phenomena of spintronics and successes can be listed in the following:

- One of the central concepts in spintronics is magnetoresistance, which refers to the change in electrical resistance in a ferromagnetic material depending on the alignment between the electric current's polarization and the material's magnetization. In particular Giant Magnetoresistance (GMR), discovered in 1988 [1], [2], is observed in multilayer structures composed of alternating ferromagnetic and non-magnetic conductive layers. The schematic representation is proposed in Fig. 1.2a and 1.2b. Moreover, Tunnel Magnetoresistance (TMR), discovered in the 1975 [3], occurs in magnetic tunnel junctions (MTJs), where two ferromagnetic layers are separated by an insulating layer (the tunneling barrier). The resistance changes depending on the relative alignment of the magnetizations of the ferromagnetic layers (parallel or antiparallel).

- Spin-Transfer Torque (STT) is a phenomenon where a spin polarized current causes dynamic change in the magnetization of a magnetic layer, potentially flipping its direction. Conversely, the dynamics of the magnetization can generate spin currents, a process known as *spin pumping*. This phenomenon is a key focus of the group, and I will describe it in more detail below.

These are just some of the relevant milestones in the field of spintronics: the progress in

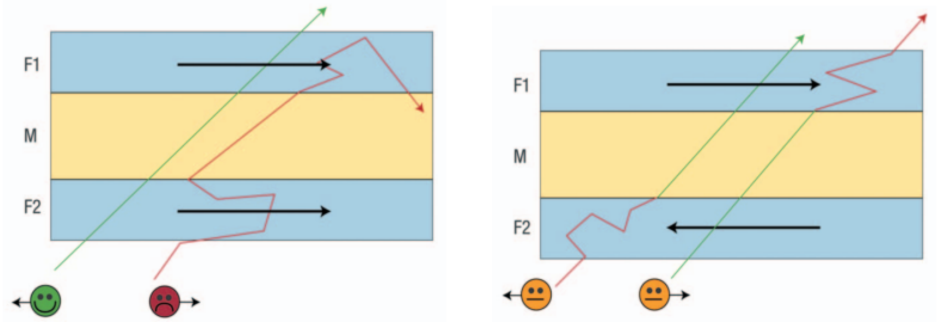

(a) **(b)**

Figure 1.2: Schematic of the mechanism of the GMR. In the parallel magnetic configuration **(a)**, the electrons of one of the spin directions can go easily through all the magnetic layers and the short circuit through this channel leads to a small resistance. In the antiparallel configuration **(b)** the electrons of each channel are slowed down every second magnetic layer and the resistance is high [4].

understanding spintronic phenomena and in the development of new technologies will lead to further innovation.

However, the performances and the efficiency of spintronic devices are mainly constrained by interface effects and significantly impacted by the interface characteristics between different materials. They are therefore crucial in spintronic devices in order to achieve efficient spin injection (poor interfaces can lead to significant spin scattering and loss, reducing the efficiency of spin injection) and accurate spin detection (detection of spin polarized currents requires clean interfaces to maintain the integrity of the spin information, since any defects or impurities at the interface can distort the signal). Moreover, as the devices are scaled down to nanometer dimensions, the surface-to-volume ratio increases, making interface effects even more important. It is therefore of great interest to switch to 2D materials rather than bulk materials [5]. Due to their unique structure, they are especially promising for high-quality interfaces. Their monolayer atomic thickness naturally prevents species diffusion and the creation of disordered alloys at the interface, resulting in nearly perfect interfaces. 2D materials, moreover, offer great tunability, flexibility and give rise to novel quantum phenomena. These advantages make them highly promising for next-generation electronic and spintronic devices [6], as well as a range of other advanced applications. Several famous examples of 2D materials illustrate the diverse and unique properties that make them advantageous. We find first graphene, single layer of carbon atoms arranged in a hexagonal lattice (Fig. 1.3a) known for its exceptional electrical conductivity, mechanical strength, flexibility, and high thermal conductivity; graphene has been shown to be an ideal material for spintronic devices due to its spin relaxation time of around 10 nanoseconds and spin relaxation length of several tens of micrometers [7]. Then among the most important materials Transition Metal Dichalcogenides (TMDs, an example is reported in Fig. 1.3b) are fundamental, since they have a layered structure with significant spin-orbit coupling, direct bandgaps, and semiconducting properties. In the end hexagonal Boron Nitride (hBN) is an excellent electrical insulator and great thermal conductor (whose structure is reported in Fig. 1.3c). We can mention also black phosphorus (phosphorene, single layer of black phosphorus with a puckered structure) and topological insulators that have insulating bulk properties but conductive surface states. These examples highlight the versatility and potential of 2D materials over the bulk counterpart.

Moreover 2D materials offer the innovative possibility to build new combinations by stacking and to discover totally new effects [8]. An example is shown in Fig. 1.3d. Such structures are obtained by putting together 2D materials by means of van der Waals (vdW) forces, that are weak forces between atoms, molecules, and surfaces.

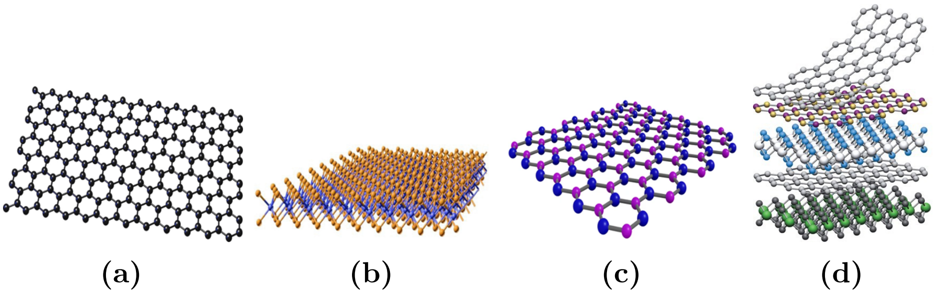

Figure 1.3: Atomic (hexagonal) arrangements for graphene **(a)**, WSe_2 **(b)** and hBN **(c)**. Example of vDW heterostructure with its building blocks [8] **(d)**.

Among the most important properties of vdW structures we find the possibility to create artificial materials and devices with greater tunability and functionalities (mechanical, electrical, thermal) e.g. combination of direct and indirect band-gap semiconductors or protection and encapsulation. They offer several unique advantages and exhibit intriguing quantum effects: first of all controlled interfaces with atomic precision and without the need for lattice matching requirements. Then also customizable band structures, bandgap tuning and enhanced mobility. For example graphene can be tuned in different phases when one layer is twisted on the other [9], [10]. Moreover, another appealing heterostructure that has been studied consists of graphene and WSe_2, such that this combination exploits the best properties of both components i.e. high mobility from graphene and strong spin-orbit coupling from the WSe_2 [11].

1.3 Objectives

This experimental internship aims to explore the technical aspects of spintronics, with a particular focus on its technological applications. The aim is to design and build elementary spintronics blocks (namely injection-propagation-detection of pure spin currents). Therefore, through a combination of theoretical approaches and laboratory experiments, fundamental phenomena related to the manipulation of electron spin and to the generation and control of spin currents are investigated, as well as the development and optimization of the techniques used. The main objectives and challenges faced during this project will also be examined, thus providing a clear picture of the state of the art of this extremely exciting research field.

The fully on-chip setup that has been realized, and that will be detailed in the next sections, is intended to inject spin through spin pumping and to transmit it through pure spin currents -in absence of a charge current- along the materials. Spin pumping is a performed when a dynamic magnetic system, such as precessing magnetization in a ferromagnet [12], injects a spin current into an adjacent non-magnetic material through exchange interaction at the interface, leading to angular momentum transfer and spin accumulation and resulting in a non-equilibrium spin density in the non-magnetic material. Moreover, an innovative detection method is represented by the inverse spin Hall effect [13] (spin to charge current conversion) and, as shown in the following, different configurations and geometries are possible. As shown in Fig. 1.4 a schematic of the device is illustrated with its three main stages: spin pumping (injection), spin propagation and spin detection.

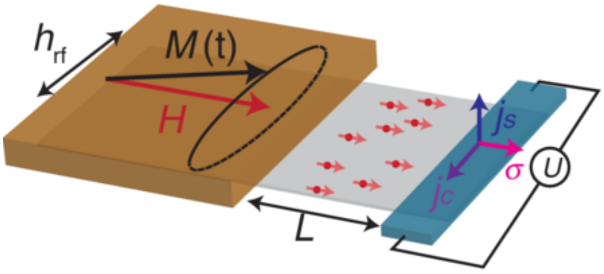

Figure 1.4: Spin pumping experiment with ferromagnetic material (brown) pumping, through precessing magnetization $\vec{M}$, a pure spin current in a non-magnetic material (grey). Propagation along the channel length L takes place in the middle. Detection is performed via Inverse Spin Hall Effect (blue contact) with conversion from spin current j_s to charge current j_c. [14].

Let us now briefly introduce some physics concepts that will be exploited in the following, as they are fundamental in the understanding of the objectives of the device and as they will help the reader during the discussion.

1.4 Elements of theory

1.4.1 Ferromagnetism

One of the most important parameters to define the properties of magnets is the *magnetic susceptibility*, that is the (dimensionless) proportional constant χ between magnetic field $\vec{H}$ -[A·m^{-1}] in S.I. units- and magnetization $\vec{M}$[1] ($\vec{M} = \chi \vec{H}$)[2].

Let us focus on ferromagnetic materials (such as cobalt, nickel, and iron) i.e. materials that exhibit long range magnetic order: the (equal) magnetic dipoles present are all parallel aligned, therefore they point in one direction only showing high levels of spin polarization. Among the most important features of such materials, we find the possibility to have a non-zero spontaneous (remaining) magnetization $\left|\vec{M}_r\right|$ when no external magnetic field is applied: this behavior is clearly visible in the hysteresis cycle present in Fig. 1.5a (magnetization curve). Saturation magnetization $\left|\vec{M}_s\right|$ (maximal magnetization of the compound) can be reached when the saturation field $\left|\vec{H}_s\right|$ is overcome, while $\pm\left|\vec{H}_c\right|$ represents the coercive field (when $\vec{M}$ compensates to 0).

---

[1] The magnetization vector is defined as the magnetic dipole moment per unit volume, i.e. the sum of all microscopic magnetic moments in the unit of volume.

[2] In non-isotropic materials, χ is a tensor and couples different directions between $\vec{M}$ and $\vec{H}$.

It is then fundamental to remark that the electronic band structure of ferromagnetic solids tends to split between spin up and spin down: this property is related to the Density Of States (DOS), that is different for electrons whose spin is aligned with local magnetization (*up* majority spin) or opposed to local magnetization (*down* minority spin), and to the asymmetry at the Fermi level[3]. In Fig. 1.5b a scheme of the density of states in a ferromagnetic metal is shown, whose d bands are shifted at the Fermi energy level E_F.

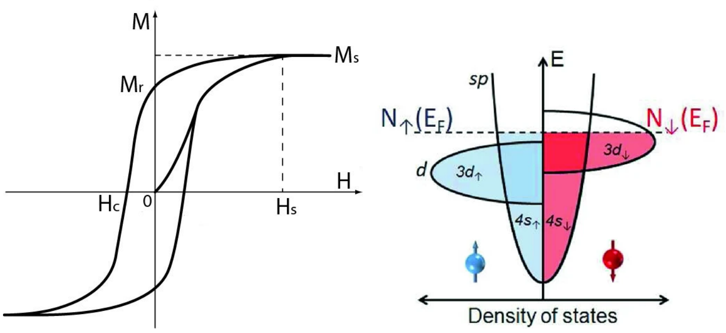

(a) **(b)**

Figure 1.5: **(a)** Hysteresis loop for ferromagnetic material. $\vec{M}_r$ is the spontaneous (remaining) magnetization at zero applied field; $\vec{M}_s$ is the saturation magnetization (maximal magnetization of the compound) that can be reached when the saturation field $\vec{H}_s$ is overcome; $\pm\vec{H}_c$ represents the coercive field ($\vec{M}$ compensates to 0). **(b)** Scheme of the density of states in a ferromagnetic metal which has d bands shifted at Fermi level E_F [15]. In 3d ferromagnetic (FM) metals, electric conduction comes mainly from 4s band electrons, whereas magnetism originates from electrons in 3d bands.

Since ferromagnetic materials exhibit an unbalance in the density of states, if we consider spin up and spin down electrons as two independent channels, this results in different conductivity for the two channels. Consequently, a charge current passing through a ferromagnetic material becomes spin-polarized.

1.4.2 Ferromagnetic resonance

When a ferromagnet (FM) is subject to a constant (DC) external magnetic field, the magnetic moments of the atoms in the material align with the field. This process occurs through the gradual rotation and alignment of individual magnetic moments with the direction of the external field, such that the net magnetization of the material increases until it reaches saturation, where all magnetic moments are aligned. When the external magnetic field varies with time (AC response), the magnetization of the FM does not simply align directly with the field. Instead, the magnetic moments exhibit more complex dynamic behavior precessing around the external field direction, gradually losing energy and aligning with the field over time. In particular, when the precession occurs at a specific frequency, known as the resonance frequency, we reach the *Ferromagnetic Resonance*

---

[3] Therefore it is possible to define the spin polarization of the DOS as the difference in the density of states at Fermi level E_F for the two spin directions $P = \frac{N_\uparrow(E_F)-N_\downarrow(E_F)}{N_\uparrow(E_F)+N_\downarrow(E_F)}$.

(FMR) condition. The resonance condition is met when the frequency of the applied electromagnetic field matches the natural precessional frequency of the magnetization vectors in the material. At this frequency, the energy from the external field is efficiently absorbed by the ferromagnetic material, leading to a peak in the absorption spectrum. To go deeper in the explanation, the magnetization dynamics is described by the the *Landau-Lifschitz-Gilbert equation* (LLG equation):

$$\frac{d\vec{M}}{dt} = -\mu_0\gamma\vec{M}\times\vec{H}_{eff} + \frac{\alpha}{\left|\vec{M}_S\right|}\vec{M}\times\frac{d\vec{M}}{dt} \tag{1.1}$$

where $\gamma = g\mu_B/\hbar$ is the gyromagnetic factor, g the Landé factor, $\mu_B = e\hbar/2m_e$ the Bohr magneton, α is the dimensionless Gilbert (phenomenological) damping parameter and $\vec{M}_S$ is the saturation magnetization. LLG equation describes the dynamics of magnetization around an effective magnetic field $\vec{H}_{eff}$ in a FM material, embedding the contributions from the external magnetic field $\vec{H}_0$, the demagnetizing field $\vec{H}_D$ and the anisotropy field $\vec{H}_K$. In the presence of Gilbert damping α, the magnetization has a spiral motion and tends to align with the applied magnetic field -as it is shown in Fig. 1.6a, where the (red) magnetization precesses around the (black) DC magnetic field in a spiral motion, due to damping-. Here we will consider the LLG equation in the presence of an external DC field $\vec{H_{DC}}$ and a small perturbative radiofrequency field $\vec{h}_{RF}$ acting as a periodic excitation. When the excitation is applied in a transverse direction of the magnetization at the specific frequency $(\gamma\mu_0\left|\vec{H}_{eff}\right|/2\pi)$, the ferromagnetic resonance can occur, coupling the external electromagnetic field with the magnetization in the FM. In the limit of an infinite plate for a ferromagnetic material with small coercivity field, the resonance condition, known as the Kittel Formula, is given by:

$$\omega_{res} = \frac{g\mu_B}{\hbar}\sqrt{H_{ext}(H_{ext}+4\pi M_S)} \tag{1.2}$$

The power absorbed in the ferromagnetic material is described by the Polder susceptibility χ" and it is represented by a Lorentz function. In general an asymmetry can be observed due to eddy currents generated by the oscillating magnetic field, distorting the resonance shape. The measured lineshape is therefore not perfectly symmetric and has an anti-Lorentzian (dispersive) contribution:

$$\chi\text{"} = A_{sym}\frac{\Delta H^2}{\Delta H^2 + (H_{eff}-H_{res})^2} - B_{asym}\frac{\Delta H(H_{eff}-H_{res})}{\Delta H^2 + (H_{eff}-H_{res})^2} \tag{1.3}$$

with A_{sym} and B_{asym} the amplitudes, H$_{res}$ the resonance field and ΔH the half width at half maximum equal to $\alpha\omega/\gamma\mu_0$. Note that the asymmetric part can be large when measuring FMR in striplines with a strong out of plane component of the RF field. The absorbed power then can be written as P$_{abs}$ $= \omega\chi\text{"}\left|\vec{h}_{RF}\right|^2$.

1.4.3 Spin pumping at FM/NM interfaces

Now let us focus on the possibility to inject pure spin from a FM at FMR condition in a Non-Magnetic (NM) one: when there is an interface with a NM material, the exchange interaction, that causes spins in adjacent atoms to align, influences the spins in the NM material thus transferring angular momentum from the FM layer. This process can be understood as the creation of a spin current that carries angular momentum. At the interface the unbalance in the density of states between spin up and spin down creates a spin unbalance in the NM layer, leading to the propagation of spin current perpendicular to the interface. This phenomenon is schematized in Fig. 1.6b, where spin unbalance at the interface is translated in pure spin current (purple) J_S directed towards the NM material. This spin unbalance in the NM layer decays over a characteristic distance known as the spin diffusion length (λ_S). Spin injection through ferromagnetic resonance can thus be viewed as the reciprocal effect to spin torque. When a spin current is injected from an adjacent layer into a ferromagnetic material, it transfers angular momentum to the ferromagnetic layer. This causes the magnetization to move out of equilibrium and start precessing and potentially flipped. Conversely, if the magnetization of the ferromagnetic layer is precessing, it will lose angular momentum to the adjacent layer. This precession results in the transfer of a spin current from the FM to the adjacent NM. The quantity which quantifies the efficiency of this spin injection technique is the *spin mixing conductance* (real part[4]), that is proportional to the difference in line width ΔH for FMR spectrum with and without the NM layer in which we pump:

$$g_{\uparrow\downarrow} = \frac{M_S d_{FM}}{\hbar f}(\Delta H_{FM/NM} - \Delta H_{FM}) \tag{1.4}$$

with d_{FM} the thickness of FM layer, $\Delta H_{FM/NM}$ the line width of the Lorentzian at FMR with the NM layer in contact and ΔH_{FM} without, M_S the saturation magnetization. Therefore the efficiency is quantified as the increase of damping at FMR (represented by the term $\Delta H_{FM/NM}$) thus measuring the additional energy loss caused by spin pumping with respect to the situation at FMR without the NM layer (ΔH_{FM}). The spin-mixing conductance describes, microscopically, the probability of spin-conserving and spin-flip scattering processes at the interface, influencing how spin-up and spin-down electrons mix together.

1.4.4 Inverse Spin Hall effect

Standard Hall effect is a magnetic effect that makes charge carriers accumulate transversely with respect to their motion due to the presence of a perpendicular magnetic field (thanks to Lorentz force); depending on their charge sign, they are deflected and they accumulate at the extremities of a sample (Hall bar), as shown in Fig. 1.7a. Here, in order to detect the presence of a pure spin current we will exploit *Inverse Spin Hall Effect* (ISHE)[5]. Spin Hall Effect (SHE) and ISHE were predicted in 1971 [17], [18]. The representation of SHE is reported in Fig. 1.7b and it consists in the spin accumulation (translated in spin current $\vec{J_S}$) on the lateral edges of a NM sample carrying an electrical current $\vec{J_C}$, the signs of the spin directions being opposite at the boundaries. No magnetic field is needed

---

[4] The imaginary part of the spin-mixing conductance can be neglected, since it is much smaller than the real part for metallic ferromagnets.

[5] Several kinds of Hall effect are present in physics (Quantum Hall Effect -QHE-, Thermal Hall Effect...) but I will not detail all of them.

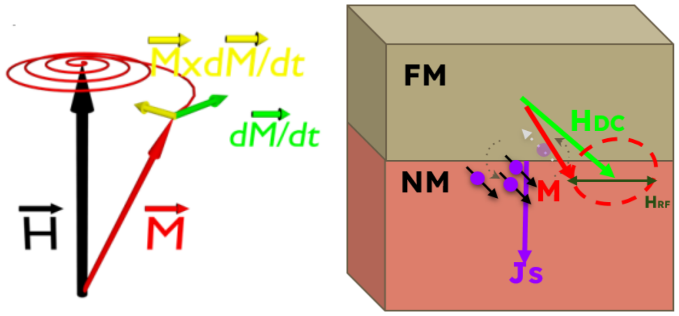

(a) (b)

Figure 1.6: **(a)** Magnetization dynamics according to LLG equation [16]. Black $\vec{H}$ is the static magnetic field that sets the equilibrium magnetization red $\vec{M}$ that precesses; green $\mathrm{d}\vec{M}/\mathrm{dt}$ describes precession motion without damping, while yellow $\vec{M} \times d\vec{M}dt$ represents the Gilbert damping that leads to spiral motion. **(b)** Spin current $\vec{J}_s$ injected due to spin unbalance at the interface from FM towards the NM material via FMR excited with RF magnetic field $\vec{H}_{RF}$.

for this phenomenon which is a purely spin-based phenomenon and it originates from spin–orbit interaction. ISHE conversely arises from the asymmetric segregation of spin up and down electrons, depending on their orientation, at the opposite extremities of a NM material, due to DOS spin dependent splitting: again, no magnetic field is involved. ISHE is depicted in Fig. 1.7c. Due to this effect it is possible to convert spin current into transverse charge current i.e. a voltage (signature of an electromotive force inside the sample) across the sample. To show this effect, material must have strong spin-orbit coupling: spin-orbit coupling indeed induces a voltage drop-electric field (translated in charge current $\vec{J}_C$) due to segregation of carriers on each side of the sample, depending on their spin direction (that is a transverse pure spin current $\vec{J}_S$). In these two effects $\vec{J}_C \propto \vec{J}_S \times \vec{\sigma}$, with $\vec{\sigma}$ the spin polarization vector.

To quantify the spin to charge conversion it is useful to use the spin Hall angle θ_{SH} for ISHE. It can be defined as the ratio between charge current density $\left|\vec{J}_C\right|$ generated perpendicularly to the spin current density $\left|\vec{J}_S\right|$ such that:

$$\theta_{ISHE} = \frac{\left|\vec{J}_C\right|}{\left|\vec{J}_S\right|} = \frac{\sigma^s_{xy}}{\sigma^c_{xx}} \frac{e}{\hbar} \tag{1.5}$$

and $\vec{J}_c = \theta_{ISHE} \vec{J}_s \times \vec{\sigma}$ where σ^s_{xy} and σ^c_{xx} are the spin Hall and the charge conductivity respectively. The inverse i.e. direct spin Hall effect angle θ_{SHE} is evaluated similarly to θ_{ISHE} but in the inverse manner: $\theta_{SHE} = \left|\vec{J}_S\right| / \left|\vec{J}_C\right|$; some examples from the literature are reported in Table 1.1[6]. Spin Hall angle is therefore a dimensionless quantity that represents equivalently the strength of the spin-orbit coupling effect in a material. Indeed we can introduce the spin-orbit length, which is the characteristic distance over which

---

[6] Al is very low spin-orbit coupling metal so it has small SH angle. Conversely, Pd and Pt are heavy metals with strong coupling.

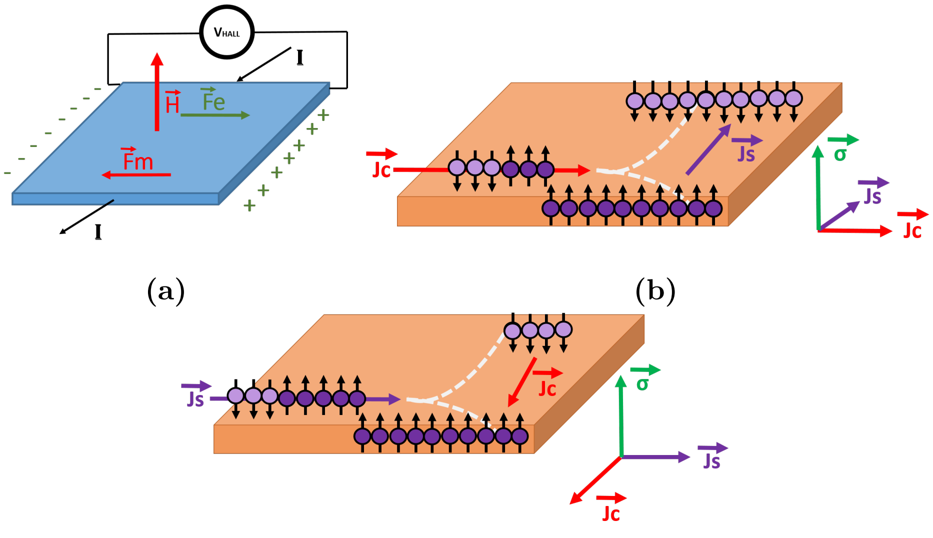

(a) (b)

(c)

Figure 1.7: **(a)** Schematic representation of (standard) Hall effect. Electrons flowing in the material are bended due to the magnetic field $\vec{H}$ (Lorentz force $\vec{F}_m$) such that they accumulate on one side of the sample. Accumulation of charge leads to electromotive force $\vec{F}_e$ and so to a voltage drop. **(b)** Schematic view of SHE phenomenon. Charge current $\vec{J}_C$ without carrying spin information generates a spin current $\vec{J}_S$ perpendicular to the spin polarization $\vec{\sigma}$ due to the segregation of different spins. **(c)** Schematic view of ISHE phenomenon. Spin current $\vec{J}_S$ (with no motion of charge) perpendicular to the spin polarization $\vec{\sigma}$ generates a charge current $\vec{J}_C$ due to the segregation of electrons by the spin-orbit coupling and therefore a voltage drop.

an electron's spin state is influenced by spin-orbit coupling. This interaction can lead to spin relaxation or dephasing, impacting the efficiency of the devices. The spin coherence length, on the other hand, is the distance over which the spin remains coherent, meaning it maintains its spin orientation. For effective spintronic device operation, it is desirable to have a long spin coherence length, allowing spins to travel longer distances without losing their orientation. The sample width plays a crucial role in these dynamics. For a device to function efficiently, the sample width should ideally be comparable to or smaller than the spin coherence length to ensure that spins maintain their orientation across the sample. However, it should also be considered in relation to the spin-orbit length to balance the effects of spin-orbit coupling and maintain desired spin transport properties.

2. Design

In my work a broadband on-chip RF current line is put under the structure and used to bring a ferromagnetic pad to ferromagnetic resonance with a magnetic-field-tunable resonance condition. At resonance, a spin current is emitted into a NM material, which can be detected either by looking at the dumped RF power, or by the ISHE voltage in a close-by electrode. Here the FMR condition is excited and analyzed, along with the potential of TMDs to replace heavy metals for spin-to-charge conversion in detecting the

Material	θ_{SH}	Ref.
Al	0.032 ± 0.006	Valenzuela, S. O.et al. 2006, Nature 442, 176
	0.016 ± 0.004	Valenzuela, S. O. et al. 2007, J. Appl. Phys. 101, 09B103
Pd	0.8 ± 0.20	Kondou, K. et al. 2012, Appl. Phys. Express 5, 073002
Pt	8.5 ± 0.9	Ganguly, A. et al. 2014, Appl. Phys. Lett. 104, 072405
Mo	-0.8 ± 0.18	Morota, M. et al. 2011, Phys. Rev. B, vol. 83, 17, 174405
$MoTe_2$	0.32	Song, P. et al. 2020, Nat. Mater. 19, 292–298
$MoTe_2$/Py	0.27	Liang, S.et al. 2020, Adv. Mater.32, 2002799
Graphene/Pt	0.15	Savero Torres, W. et al. 2017, 2D Mater. 4, 041008

Table 1.1: Spin Hall angles from experimental measurements.

spin currents. These devices are crafted from single-layer 2D materials obtained through dry transfer technique from pristine crystals, and subsequently built through different lithography and metal deposition steps.

The device has been designed starting from the work of the PhD student that follows me during the project. It is shown in Fig. 2.1a and I independently fabricated it in cleanroom environment with several techniques that will be described in next sections.

The idea is to achieve spin pumping and electrical spin current detection: a thin film of cobalt (the FM material) is put on top of the target heavy[1] 2D material -namely tungsten-diselenide (WSe_2)-, while a magnetic field is applied through the structure in order to excite the spin pumping from top to bottom. A static magnetic field (green $\vec{H}_{DC}$ in the picture) sets the equilibrium magnetization in FM, while a microwave component ($\vec{H}_{RF}$) leads the magnetization (red $\vec{M}$) to precess. To get such a configuration a gold microwave microstrip is used: a RF current passes through the strip such that its Oersted field generated the small oscillating component. The structure is posed directly on top of the strip to maximize the coupling and get the maximum intensity. Therefore on top of the strip we place the different materials i.e. hBN (to insulate electrically the gold RF line from the structure above, whose thickness is the less relevant), WSe_2 (due to its strong spin-orbit coupling) and then cobalt on top of it. The choice of the thicknesses is directly related to the different length scales involved. First we want to test the spin orbit length in WSe_2, thus putting it directly in contact with cobalt we exploit its strong spin-orbit such that the spin current is directly converted into a charge current by ISHE.

However I had also the possibility to build another kind of device that is a step further, in which spin propagation is involved: in such a device (shown in Fig. 2.1b) the structure involves the same components but at the end of the propagation channel -WSe_2- a strong spin-orbit heavy metal -palladium, which is a standard metal for ISHE [19], [20], [21], [22]- is exploited for the ISHE detection and the main parameter is the spin diffusion length in TMDs.

Therefore in the second configuration that has been investigated in the current work a palladium bar is placed at a fixed distance from the cobalt and on top of the WSe_2, to let the spin current propagate and let the ISHE create the electrical current needed to detect the segregation of spin. The distance between cobalt and palladium has to accommodate

---

[1] Experimentally spin-orbit coupling is proportional to the fourth power of the atomic number Z^4.

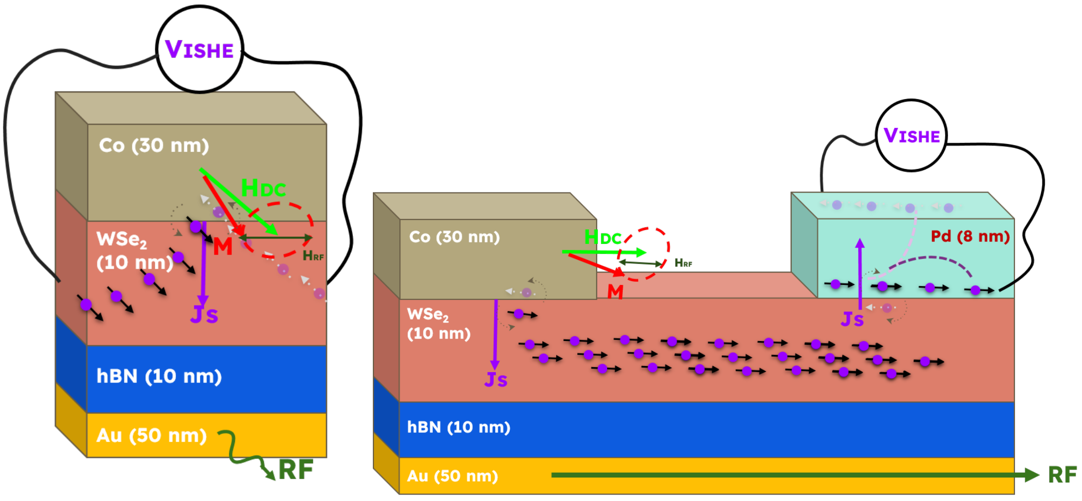

(a) (b)

Figure 2.1: **(a)** Schematic of the device I built. Thickness is not in scale. Cobalt is the ferromagnet intended to excite spin pumping due to FMR while WSe_2 is the heavy material that exploits its strong spin-orbit coupling to let charges segregate and measure ISHE voltage. To insulate I exploit hBN between the structure and gold RF line. **(b)** Schematic of the second configuration I built. Thickness is not in scale. Along WSe_2 the spin current propagates, then diffuses in palladium bar, that exploits its strong spin-orbit coupling to let charges segregate and measure ISHE voltage.

the spin propagation (relaxation) length λ (time τ); we use a standard distance of 400 nm and see if we get any signal. Then another important figure of merit to evaluate is the efficiency of the spin to charge conversion that is represented by spin Hall angle for WSe_2 and palladium: the goal is to compare the two and see which material shows a better and more efficient spin to charge conversion.

To obtain such complex structures, several fabrication techniques are exploited, starting from the beginning i.e. patterning the bare wafer up to the very last lithography and deposition steps, that will be detailed in the following sections. The devices presented here are fabricated on 200 nm of silicon dioxide (SiO_2) on top of 380 μm thick intrinsic silicon (Si) to reduce RF losses. Once the main gold DC contacts are obtained, as well as the microstrip (Sec. 3.1), hBN is deposited on top of it; then WSe_2 is deposited as well by using the same exfoliation (Sec. 3.2) and dry transfer techniques (Sec. 3.3); the last bunch of steps require successive electron beam lithography session (Sec. 3.4), in order to define the correct geometry and patterning of the different materials (namely Co, Pd and Au), and right after metallic deposition (evaporation, Sec. 3.5).

3. Nanofabrication

In this chapter I will describe the most important nanofabrication techniques involved to assemble the device from the very beginning, in order to understand how the structure is built, the choice of the materials and the difficulties encountered during the process. I will follow in parallel the fabrication of the two configurations of devices i.e. the one composed solely by cobalt on WSe_2 and the one with propagation along the WSe_2 channel with palladium bar on top of it and distant from cobalt. Both devices as already said are put on hBN and gold RF antenna.

I will not report each step of cleaning of the wafer, that are performed in acetone and then in isopropanol (IPA), neither oxygen plasma step that may be needed to eliminate further organic residues.

3.1 Photolithography

Lithography is the very first step involved in this project: it is the process by which circuit or device patterns are transferred from layout to substrates, and it has been developed since we cannot directly grow neither deposit films only in desired areas (selective processing). In particular, *photo*lithography is the technique used to transfer a desired pattern from a master copy (or mask) into a polymer layer, called photoresist[1], on the wafer surface. The patterned polymer layer is used to protect areas of the wafer during etching – or pattern transfer/deposition. After cleaning the substrate –to remove particles on the surface as well as any traces of organic, ionic, and metallic impurities-, the next step is the spin-coating of the resist[2] on the wafer; then the alignment and exposure are performed; in the end the development of the resist eliminates either the exposed ares (if positive[3]) or the unexposed ones (if negative[4]). The working principle of photolithography is illustrated in Fig. 3.1.

Let us now briefly describe the pattern that is used to built the main area of interest i.e. the DC contacts for current measurements and contemporarily the RF antenna, that drives the samples to resonance. The structure can be realized both with photolithography and with electron beam lithography, but in the following we will detail the second option. The pattern requires a 10 μm wide - 50 nm high gold microstrip, long enough to accommodate as many devices as possible. DC contacts are placed on the sides of the line, to make the useful connections in the end and to be able to measure DC voltage.

Therefore our very first step consists in covering a Si-SiO_2 wafer with the main circuit by UV lithography. First a pre-designed (by Karen Sobnath) mask is used, and it is shown in Fig. 3.2, whose unexposed areas are covered by chromium instead of being made of glass (transparent). The machine performs UV lithography whose source is provided by a nitrogen cooled UV lamp. We investigated both the Vacuum Contact (VC) and Hard Contact mode i.e. the sample is directly in contact with the mask allows to reduce

---

[1] Photoresists are photosensitive organic mixtures which contain polymer resins (a binder that provides mechanical and chemical properties, adhesion, thermal stability ...), photoactive compounds and solvents (that control the viscosity of the base).

[2] Spin-coating is a method for applying a uniform thin coating onto a flat substrate. The coating material on the substrate can spread evenly over the surface through centripetal acceleration forces. Based on spin curve, it is possible to determine optimum spin speed (revolutions per minute) and target thickness for a certain photo resist.

[3] Light breaks the polymer chains to make them more soluble in the developing solution.

[4] Light induces cross-linking of the polymer chains to make them less soluble in the developing solution.

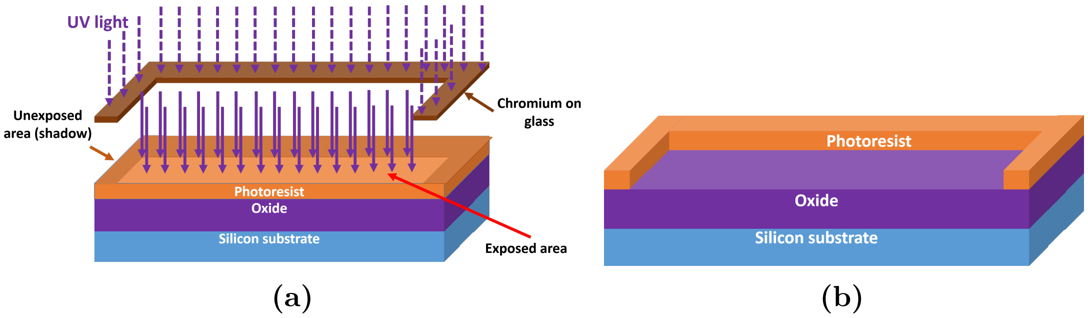

Figure 3.1: Working principle of positive resist. The glass let UV light pass and expose the resist, whose polymeric chains are broken, while light cannot pass through the chromium areas, making the shadowed areas unexposed **(a)**. After the development **(b)**, the soluble (exposed) part goes away, leaving only the unexposed resist. The inverse happens for negative resist (whose polymeric chains are strengthened and no soluble after development).

the diffraction limitation of such procedure[5]. The resist used here is *AZ 5214 E* (whose spin-coating parameters are reported in Table 3.1) and its developer is *AZ 326 MIF*[6], for which two exposures -Fig. 3.3a and 3.3d- and a baking -Fig. 3.3c- are performed. The advantage of this technique is that, by doing a reversal bake (60 seconds at 120°C) in between the two different exposures (0.9 seconds vs 60 seconds of *flood* exposure), we can actually reverse the slope of the image sidewalls, such that it can facilitate the resist removal (lift-off) in acetone. Relatively high thickness resist is usually needed and the deposited film thickness has to be lower than the resist thickness.

Cycle	**Speed (rpm)**	**Time (s)**
1	500	3
2	4000	30

Table 3.1: Spin-coating parameters for *AZ 5214 E* photoresist.

---

[5] Nevertheless, many disadvantages are presents, like mask-wafer contact can lead to contamination, does not allow any magnification and since the mask is usually the same size as the wafer, larger samples cannot be exposed.

[6] 40 seconds are spent in the developer, then 40 seconds in water.

Figure 3.2: Optical mask used to design the pattern. In the center the microstrip, around the DC contacts. The brown areas (unexposed) are chromium.

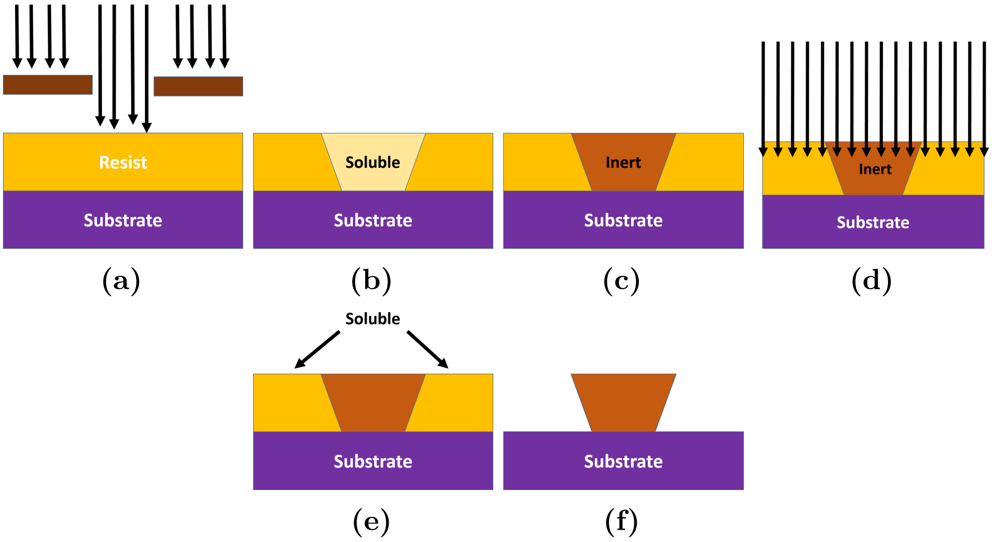

Figure 3.3: UV lithography performed along with reversal bake step and flood exposure. A negative resist becomes positive and ameliorates the lift-off procedure. From **(b)** to **(c)** reversal bake at 120°C for 60 seconds is performed, reversing the resist functioning. **(f)** is after the development.

After this step, the, gold is deposited in the selected areas (for the metal deposition details, see Sec. 3.5).

3.2 Exfoliation

The second step, once the gold has been deposited, consists in exfoliating both hBN and WSe_2 bulk samples to obtain thin flakes, that are inspected by optical microscopy. Mechanical exfoliation basically consists in removing -ideally- layer by layer the material starting from the bulk[7]. The idea here is to find large enough hBN flakes that can

---

[7] Let us recall that this technique lead to the discovery of graphene in 2004 by K. S. Novoselov and A. K. Geim [23] starting from bulk graphite.

accommodate the whole structure and that can attach to the SiO_2 at the same time (so at least 15 μm by 15 μm); the same rule applies for WSe_2, to be as large as the strip (10 μm) and long enough for cobalt sample and possibly for palladium bar. The flakes are exfoliated by using PDMS scotch-tape-like pieces, that provide the proper stickiness, onto p-doped silicon wafer (with 300 nm SiO_2 on top, to provide the correct contrast under the microscope)[8]. These flakes will be transferred onto the chip with hot pick-up technique described in the following section.

3.3 Hot pick-up

This technique is very crucial in the whole process flow. It consists in the dry transfer of 2D flakes from a substrate onto an other one [24], [25]. We use a glass slide with a Polydimethylsiloxane (PDMS) drop[9] on top. The solution of the drop, once dried, is covered with a Polypropylene Carbonate (PPC) solution (diluted with anisole[10]) to give the drop the proper adhesion. PPC is spin-coated on PDMS drops according to the parameters reported in Table 3.2 The pick-up of hBN and WSe_2 flakes is performed at 60°C, while the drop-down is performed at 90°C, to let the interactive forces between the flake and the material underneath be enhanced and to facilitate the release. Some examples of flakes targetted and transferred onto the Au line are shown in Fig. 3.4, while the schematic representation of the various steps is proposed in Fig. 3.5.

Cycle	Speed (rpm)	Time (s)
1	500	5
2	2500	30

Table 3.2: Spin-coating parameters for PPC on PDMS drops.

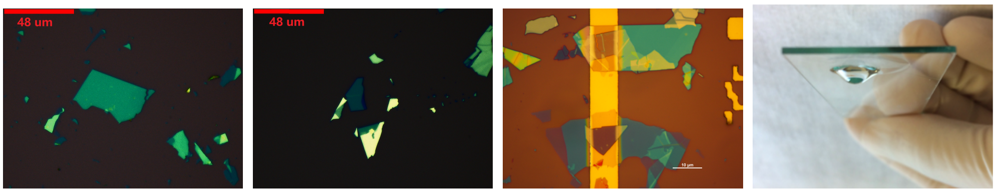

(a) **(b)** **(c)** **(d)**

Figure 3.4: Exfoliated hBN **(a)** and WSe_2 **(b)** flakes targetted for dry transfer technique (scale bar on top left is 12 μm). Transferred hBN and WSe_2 flakes onto the Au antenna **(c)** (scale bar on bottom right is 10 μm); several devices (flakes) are put in series to collect the highest possible ISHE signal. PDMS drop on glass **(d)**.

---

[8] This step is very useful in order to find flakes to be at at least 15 nm thick. This thickness provides a good contrast also in the pick-up.

[9] The solution is prepared by using a silicone elastomer base mixed with a curing agent. The ratios that have been used are 1 part of curing agent over 10 of elastomer and also 1:9.

[10] With ratio 1.5 g of PPC and 10 g of anisole.

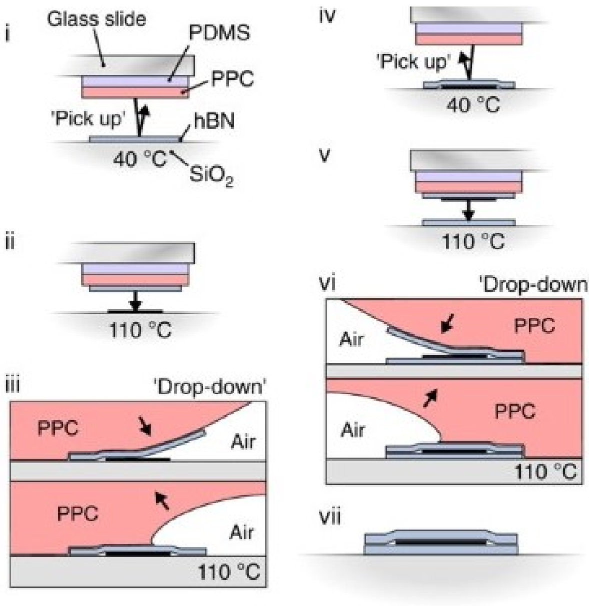

Figure 3.5: Schematic representation of needed steps in pick-up to build an heterostructure [24]. In this work I pick-up hBN and put it onto the gold RF antenna; then pick-up WSe$_2$ and drop it down on top of hBN, such that it is insulated with respect to the antenna.

3.4 Electron beam lithography

This kind of lithography uses a focused beam of electrons instead of light to expose radiation-sensitive resist; moreover, I exploit Electron Beam Lithography (EBL) for direct writing and therefore the resist is Poly(methyl-methacrylate) (*PMMA*)[11] whose spin coating parameters are reported in Table 3.3; here I use a bilayer of PMMA[12] and the correspondent dose is reported in Table 3.4. The developer for this kind of resist is MIBK diluted in IPA with ratio 1:3[13].

Cycle	Speed (rpm)	Time (s)
1	500	3
2	4000	40

Table 3.3: Spin-coating parameters for both the two layers of *PMMA*. First is PMMA 50k pure, the second is PMMA 950k A6 diluted in anisole with a ratio of 4:1. After each spin-coating, 1 minute baking at 180°C is needed.

Electrons are exploited due to their wave-like nature and due to the fact that, when accelerated in a focused beam, their can reach high velocity (low wavelength) so high

---

[11] It is a positive resist used for short wavelength lithography and used to achieve very high resolution and low sensitivity.

[12] First a dehydration bake of at least 10 minutes at 120°C is needed to clean the sample from every acetone and IPA residues.

[13] 20 seconds, then 20 seconds in IPA.

energy to expose the resist. The procedure is highly automatized and precisely controlled and no mask is involved: the pattern is designed on a software (*PIONEER Two*) and transferred to the machine. The sample is just put in vacuum and properly aligned, to then proceed with the exposure. During my project I had to exploit EBL to reach very high precision in order to deposit cobalt and palladium on top of WSe_2 and then to connect either palladium bars or WSe_2 to the DC contacts. On the software, it is only needed to draw the pattern and select the corresponding layer of exposure (cobalt, gold, palladium) as shown in Fig. 3.6; one has to select also the correspondent dose. The most important parameters for this step are reported in Table 3.4:

Dose	Step-size	EHT	WD	Aperture	WF
240 μC/cm^2	0.016 μm	10 kV	10 mm	20 μm	637 × 100 μm

Table 3.4: EBL parameters. EHT is the accelerating voltage, WD is Working Distance, WF is Writing Field.

Moreover, one of the most important features of this technique is the use of alignment marks. Since the only signal that can be exploited is represented by electrons (the sample is kept under vacuum with no optical microscopy source), and each electron could expose the resist in an unwanted manner, it is fundamental to align with the highest precision possible the chip with respect to the mask. Here it is done thanks to alignment crosses that are placed at the corners of the 4 working areas in which the strip is divided and that were deposited with gold at the beginning, after the photolithography step. An example is shown in Fig. 3.9, in which the red dashed box highlights the working area, set by the presence of alignment crosses at the corners (red arrow).

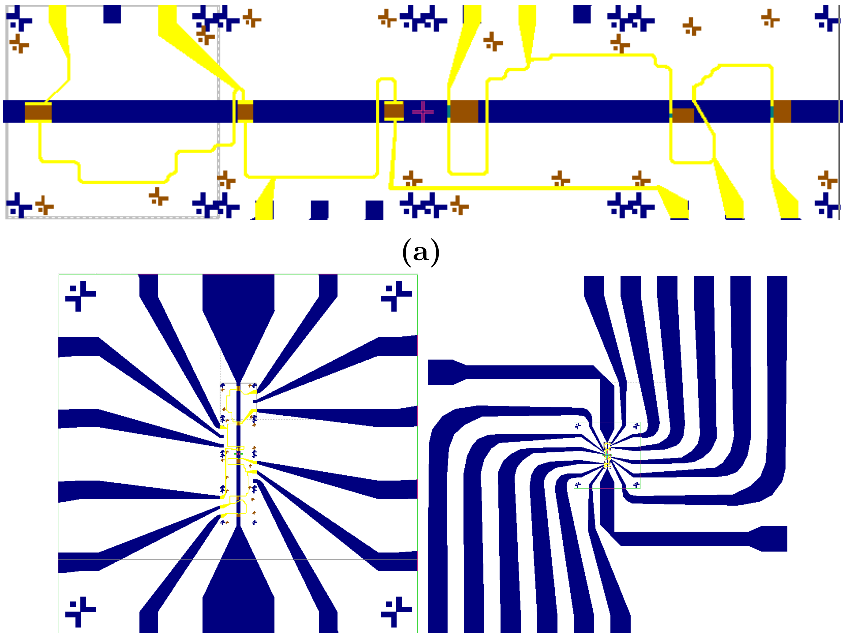
(a)
(b) **(c)**

Figure 3.6: Design of the optical mask used for EBL, done in PIONEER Two. RF line and DC contacts (blue) with brown Co, grey Pd and yellow Au for DC contacts represent different layers in **(a)** (rotated by 90°), **(b)** and **(c)**. 4 working areas didvide the microstrip design.

3.5 Metallic evaporation

During this step we deposit the target metal on the substrate. Metallic evaporation is a form of Physical Vapor Deposition (PVD[14]), where metal is evaporated in vacuum[15] and then condensed onto a substrate to form a thin film. The process involves a metallic source i.e. the material to be deposited is placed in a crucible which is then heated to a high temperature. This can be achieved through resistive heating, electron beam heating, or laser heating, but here we will refer to the second type of heating: an electron beam -accelerated by a voltage and deviated with a magnetic field- is directed from the filament at the metal source, causing localized heating and evaporation (see Fig. 3.7a). This method can achieve higher temperatures, it is suitable for metals with high melting points and high deposition rates can be reached. Then once the metal reaches its evaporation temperature, it transitions from a solid to vapor phase. The substrate is positioned above the evaporation source, directly facing it. The metal vapor condenses onto the substrate, forming a thin, uniform film (Fig. 3.7b). Starting from the rate (nm/s) of deposited material, the correspondent thickness is calculated based on a quartz oscillating scale.

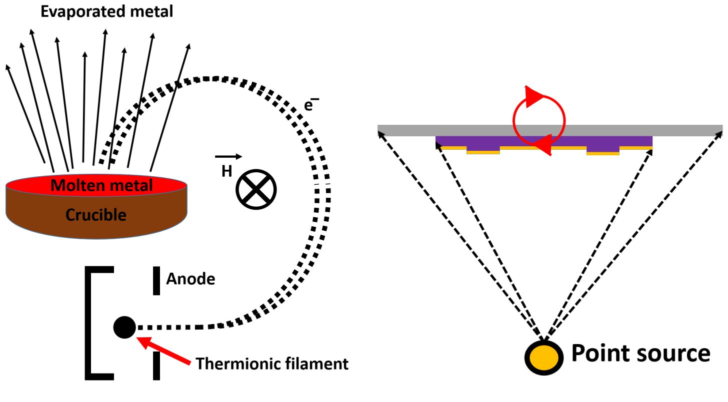

(a) (b)

Figure 3.7: Metallic evaporation performed with electron beam is shown. Electrons are accelerated by a voltage and deflected by perpendicular magnetic field ($\vec{H}$) onto the crucible, that contains the target metal. Once heated above the melting point, it starts to evaporate and the cone of emission let the material to go on the substrate **(a)**. Once the material evaporates, it condensates on the (purple) substrate; since the cone of emission is not isotropic, the substrate rotates (red circle) to let the deposition be homogeneous **(b)**.

During the project, the first step involved deposition of 50 nm of gold (on 5 nm of titanium, to increase the adhesion on silicon dioxide) for RF line and DC contacts (just after the photolithography step described in Sec. 3.1); then 30 nm of cobalt on WSe_2 flakes (with 2 nm of gold on top to avoid oxidation); 8 nm of palladium (and 2 nm of gold on top again); in the end, to connect the structure to the DC contacts, 150 nm of gold (on 5 nm of titanium) patterned again with EBL as for Co and Pd (Sec. 3.4). The whole list of parameters are reported in Table 3.5. In the very end of the process, it is

---

[14] Film growth achieved by the accumulation (condensation) of a vapor onto a cooler substrate.

[15] The process is carried out in a vacuum chamber to prevent contamination from air and to allow the metal atoms to travel undisturbed from the source to the substrate.

needed to perform the lift-off of the unwanted deposited areas. The steps are schematized in Fig. 3.8, where acetone dissolves and removes the resist on top of which the metal has been deposited; by doing so, the desired areas are left on the substrate. Sometimes it is useful to scratch a bit the edges of the wafer with a cotton pad to help acetone diffuse and remove the resist, as well as the creation of fluid flow with a syringe to remove it fast. In Fig. 3.9b an optical picture shows the final sample with many device on the RF line in series.

	Ti	**Au**	**Co**	**Au**	**Pd**	**Au**	**Ti**	**Au**
Thickness (nm)	5	50	30	2	8	2	5	150
Rate (nm/s)	0.05	0.05	0.04	0.04	0.04	0.04	0.05	0.07

Table 3.5: Metallic evaporation deposition parameters for different metals (deposited in sequence starting from left to right).

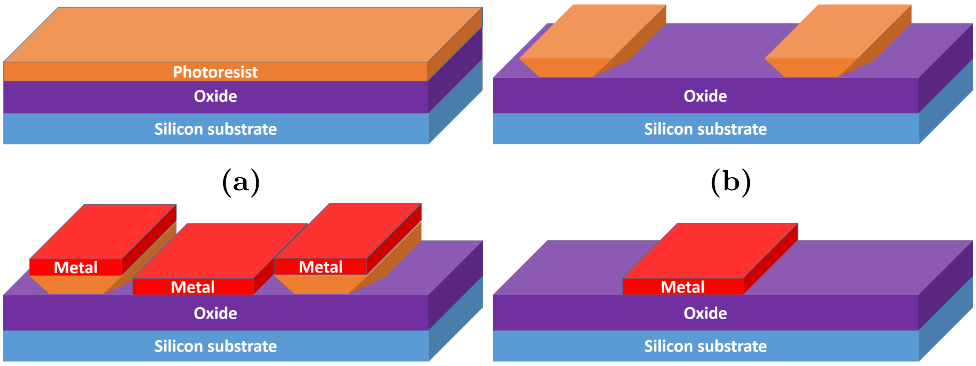

(a) **(b)**

(c) **(d)**

Figure 3.8: Lift-off procedure to remove the resist on top of which there is deposited metal. Photoresist deposited on the substrate **(a)**; after the lithography procedure **(b)** metal is deposited on the whole area **(c)**. In the end the residual resist is removed **(d)** by using acetone, that passes easily leaves just the wanted metal piece.

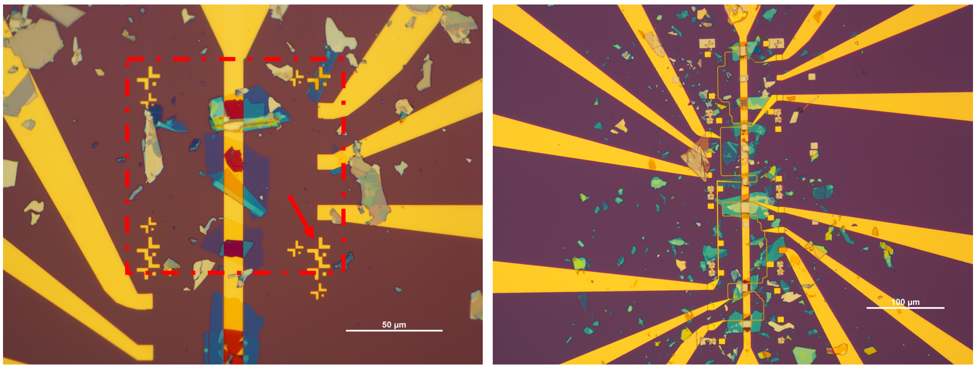

(a) **(b)**

Figure 3.9: **(a)** Partial optical image of few devices before EBL. Red dashed box highlights the first working area, set by alignment crosses at the corners (red arrow). On left and right DC contacts. **(b)** Optical image of final device: 6 devices are placed in series, first 3 starting from upper part involve no Pd bar, while last 3 do.

4. Atomic force microscopy

In this section we review the most important results retrieved by using the Atomic Force Microscopy (AFM) onto the samples, in order to determine the thickness of the layers utilized as well as their roughness and homogeneity. AFM is a powerful and versatile imaging technique used to analyze surfaces at the nanoscale. It provides high-resolution and three-dimensional images of a sample's surface. This technique uses a cantilever with a sharp tip at its end. The tip has a radius of curvature in the nanometer range to let the interaction with atoms on the surface be the maximum possible. When the tip is brought close to the sample surface, forces between the tip and the surface (vdW forces and electrostatic forces) let the cantilever to deflect. A laser beam is focused on the back of the cantilever and the reflected beam is detected by a photodiode, which measures the deflection of the cantilever. A feedback loop maintains a constant force between the tip and the sample by adjusting the height of the cantilever. This allows the AFM to scan the surface in a controlled manner; see Fig. 4.1 for schematic representation of AFM stage. As the cantilever scans across the sample surface, data from the photodiode is used to construct a topographical map of the surface. Moreover, it can operate in several modes: contact mode, in which the tip is continuously in contact with the sample surface, and non-contact mode, in which the tip oscillates above the surface without making contact.

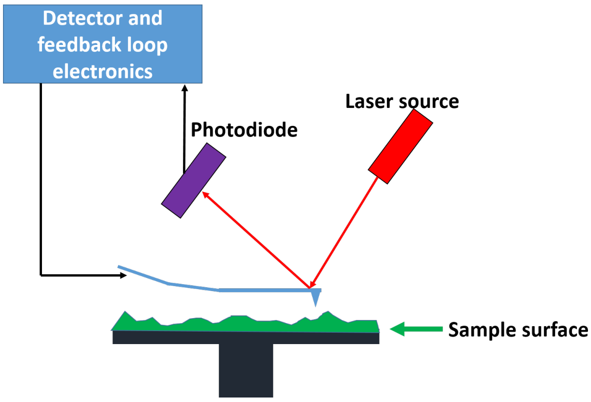

Figure 4.1: AFM schematic. The working principles are shown: the tip approaches the sample surface, forces between the tip and the surface let the cantilever to deflect and laser beam focused on the back of the cantilever is detected by a photodiode, which measures the deflection. A feedback loop reads the input and adjusts the cantilever height.

In my work I exploited AFM in non-contact mode such that the cantilever is driven to oscillate at or near its resonance frequency. The idea is to determine the thickness of the flakes that have been exfoliated and then deposited, and the thickness of the evaporated metals. In the following various results are reported. The main signal coming from AFM machine is represented by a voltage (used to drive the piezoelectric stage that moves the tip) and so by the correspondent height from the sample; in the following I will look mainly at the z signal coming from the microscope in forward scanning. In particular, I performed AFM analysis on the devices involving palladium bar on WSe_2, to have a complete description of hBN and WSe_2 flakes -thickness, homogeneity and defects-, cobalt and palladium. Moreover, AFM is a very useful tool that can help to determine the distance between cobalt and palladium and see if it corresponds to the fixed (400 nm) distance set by EBL. In Fig. 4.2 different 3D pictures are available for this kind of structure and they focus on the cobalt-palladium gap of one specific device. We can observe the rugosity and roughness of the structure and massive presence of air bubbles.

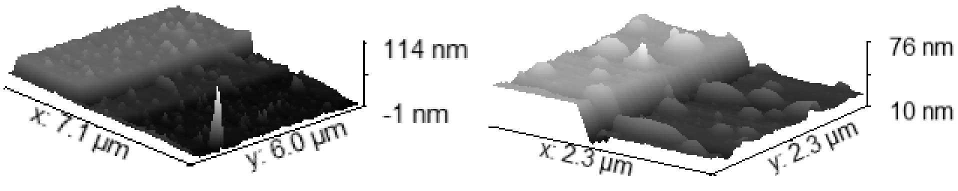

(a) **(b)**

Figure 4.2: The device that is shown presents cobalt and palladium on WSe_2 starting from left to right (steps) **(a)** and a zoomed image that focuses on the dip between Co and Pd **(b)**.

It is clear then, by looking at the pictures, that the whole structure presents air bubbles that, starting from the pick-up step, could stay and remain until the last step of fabrication. These kind of bubbles could be removed in principle by performing an annealing step, by leading them to segregate and expelled from the edges of the flakes; however the disadvantages of this technique can lead to coalescence in bigger bubbles so it is not a reliable method. The idea should be instead to perform pick-up and drop down of hBN and WSe_2 paying attention to the air incorporated e.g. flattening the PDMS drop and melting it.

Let us now review some results from the pictures reported above. From the software that analyzes the data (*Gwyddion*) retrieved from the microscope, it is possible to select the desired profile from the image and extract a plot: the idea is to plot different steps of cobalt, WSe_2 and hBN and determine the thickness. As shown in Fig. 4.3, it is possible to look at the profile Co-Pd on WSe_2 (4.3a) and, more importantly, at the gap between Co and Pd (4.3b). On left cobalt is more than the nominal 30 nm thick ($\simeq 40nm$), while on right the palladium is at least 10 nm[1]. It is moreover clear that a gap is present between the two materials and it is not just an artifact from the tip (due to the presence of the gap even in the reverse scanning and not only in the forward one). However, it is difficult to quantify such distance between Co and Pd, since the precision (size) of the tip does not allow any further analysis. Target distance is 400 nm, but probably the two are closer.

Let us now see if it is possible to retrieve the thickness of the deposited 2D materials. Let us inspect Fig. 4.4: first, in Fig. 4.4a we can observe the whole profile of WSe_2 on hBN on Au (0 level); if we inspect more carefully the profile, we can plot the single steps and fit the data such that we can obtain a thickness for both WSe_2 and hBN. That is done in Fig. 4.4b and 4.4c, respectively: in the first picture WSe_2 on hBN profile is analyzed and

---

[1] This discrepancy between the nominal value and the actual thickness can be attributed to the evaporator machine that deposited more material than expected.

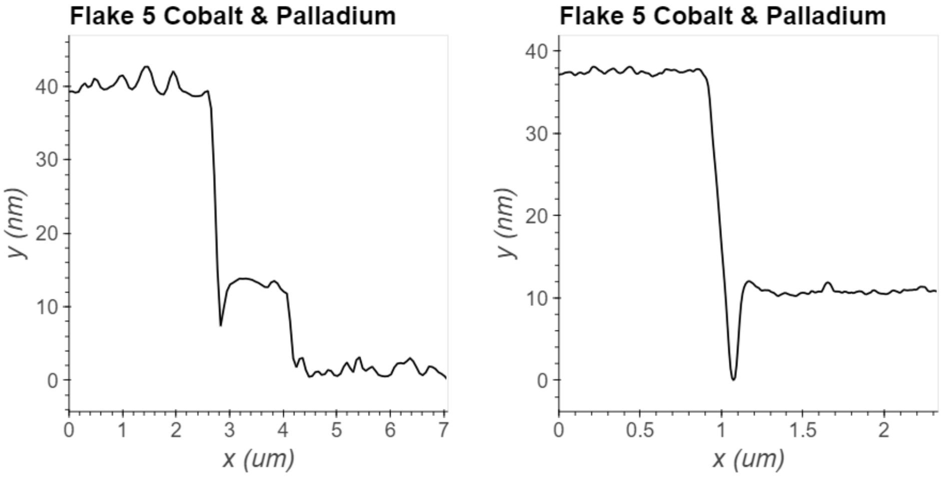

(a) **(b)**

Figure 4.3: The picture shows the profile for Co-Pd (on WSe_2), whose gap in between separates them. **(a)** Data normalized such that the minimum height (represented by the WSe_2 level) is 0 nm. Co on left, Pd in the middle, WSe_2 on the right as the reference level. **(b)** Again Co on left, Pd on right

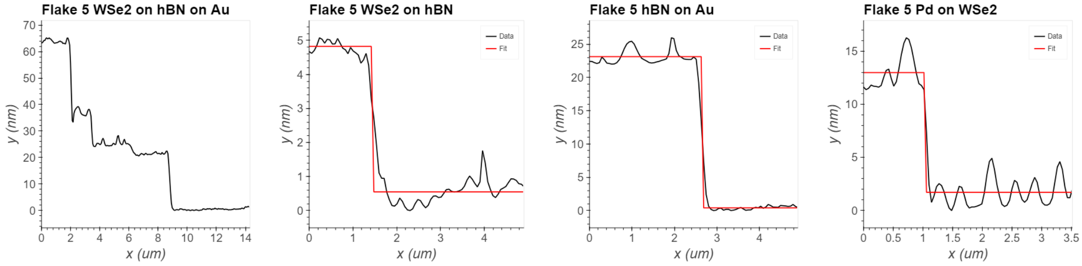

(a) **(b)** **(c)** **(d)**

Figure 4.4: **(a)** AFM profile for the whole structure i.e. Co near Pd on WSe_2 on hBN on Au; different profiles for various materials: **(b)** WSe_2 (left) on hBN (h = 4.2761 nm ± 0.38 nm), **(c)** hBN (left) on gold (h = 22.736 nm ± 1.2 nm) and **(d)** Pd (left) on WSe_2 h = 11.27 nm ± 2.1 nm, with correspondent fits to a step function. Data were normalized such that the minimum height for each picture is 0 nm.

the fit gives a height h equal to 4.2761 nm ± 0.38 nm of uncertainty, while in the second picture hBN on Au gives a thickness equal to 22.736 nm ± 1.2 nm. This represents a very important result, since it means that we picked up very thin flakes of WSe_2 and quite thick hBN flakes. As already stated, the thickness of hBN is the less relevant in the heterostructure since it just serves the insulation from RF line; however the thicker hBN is, the weaker the coupling between RF line and cobalt (in terms of microwave magnetic field $\vec{h}_{RF}$) will be. In the very last picture it is possible to establish precisely the thickness of Pd bar on WSe_2, that is equal to h = 11.27 nm ± 2.1 nm that is, again, greater than the target value > 8 nm.

5. Results at FM/2D interfaces

The last step consists in performing FMR and ISHE measurements. The sample is eventually placed on the sample holder, and ultrasonic micro-wire bonding is used to connect it -including the antenna and DC contacts- to the Printed Circuit Board (PCB).

5.1 Experimental setup and lock-in technique

As shown in Fig. 5.1 the sample holder is put in the experimental setup: it is therefore positioned between two magnetic coils that generate a magnetic field to align the magnetization of the ferromagnetic material along the strip. The microwave power emitted from the device is measured and DC voltages are measured also, across the DC contacts of the chip and through filtered lines (whose characterization is detailed in Appendix A) to filter out higher-frequency noise. More in detail, the results that will be described in this chapter are performed using the *lock-in technique*. The lock-in technique is used to extract weak signals from noisy environments by leveraging a carrier wave with a known reference frequency. It involves using a reference signal, typically a sinusoidal wave, which is then multiplied with the noisy input signal. This process shifts the frequency of the desired signal, making it easier to isolate. A low-pass filter is then applied to remove high-frequency noise, leaving the DC components that are proportional to the signal amplitude. The phase and amplitude of the original signal are in the end determined by recombining the in-phase and quadrature components. In this project the lock-in method modulates the magnetic field applied to the device under test $H + \delta H(t)$ at very low frequency (< 50 Hz) with respect to the RF signal and gives an output (voltage) proportional to the desired signal. As shown in Fig. 5.1, we inject RF power i.e. AC current in the line with a microwave source allowing the control of the applied frequency and power and then the magnetic field is applied. The sample holder is placed between a Bias-T[1] and a DC-block on the two sides such that it is possible to control independently the DC electric potential of the central microwave line. It could allow us to apply static gate voltage to the microstrip and possibly tune the signal, as far as free charges are injected. Two outputs are recorded: from the RF line a diode converts the signal into a voltage, multiplied with the lock-in reference signal such that the output is proportional to the derivative $\frac{dP_{out}}{dH}$; the same happens for the voltage V_{ISHE} across DC contacts, whose output is proportional to $\frac{dV_{ISHE}}{dH}$.

5.2 FMR measurements

Let us first see the outcome of FMR measurements. Color-plot of FMR condition is shown in Fig 5.2a, where derivative of absorbed power P with respect to magnetic field

---

[1] Bias T allows the decoupling of RF input (capacitance closed, inductance opened) from independent DC source (capacitance opened, inductance closed) e.g. gate voltage.

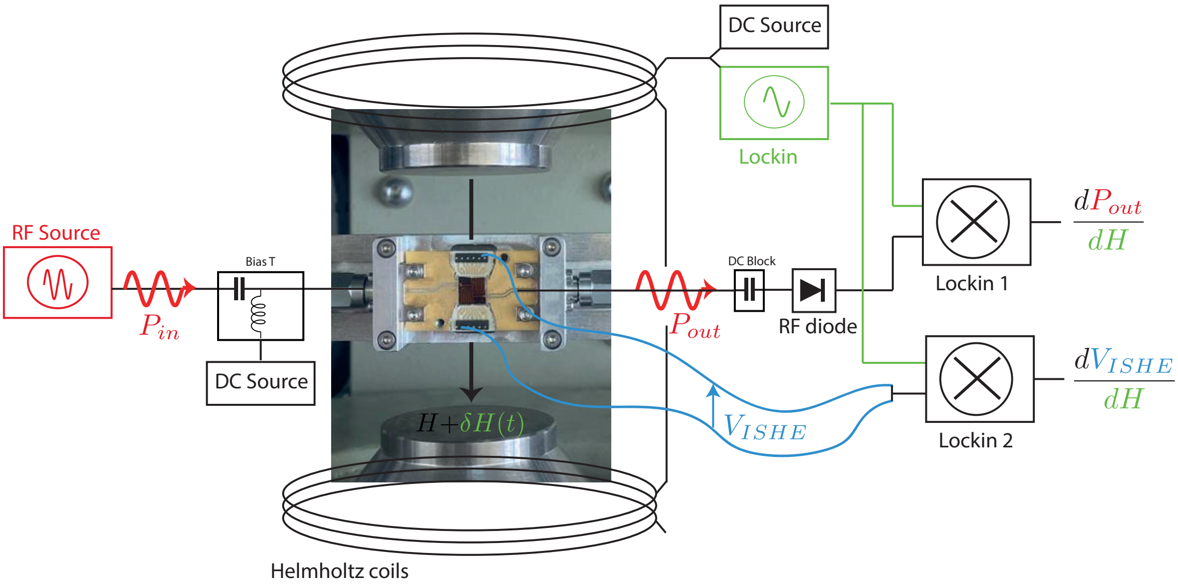

Figure 5.1: Sample holder with the chip glued on it along with the PCB wire-bonded to it. Helmholtz coils apply static magnetic field H plus modulation δH(t) according to the lock-in reference signal at very low frequency. RF source injects AC current in the line, output power P_{out} is collected by RF diode, which converts the signal in voltage. Bias-T (left) and DC-block (right) allow us to control independently the DC potential of the line and the RF current. Multiplier (*Lockin 1* in figure) combines the signal with reference frequency, giving the output proportional to $\frac{dP}{dH}$. ISHE voltage V_{ISHE} is collected by *Lockin 2* multiplier and the output $\propto \frac{dV}{dH}$.

H (magnitude) is plotted as a function of both *H* and frequency *F*. Black dots represent resonance frequencies fitted with derivative

$$\frac{dP}{dH} = K\frac{4(\delta H/\Delta H)}{(1+4(\delta H/\Delta H)^2)^2} + \Delta K\frac{1-4(\delta H/\Delta H)^2}{(1+4(\delta H/\Delta H)^2)^2} \tag{5.1}$$

of Lorentzian function that was given in Eq. 1.3, where K is the amplitude of the symmetric part, ΔK the amplitude of the antisymmetric part, δH is H_{ext} - H_{res} (the external magnetic field is the only contribution to effective field H_{eff}), H_{res} the resonance value and ΔH the half width at half maximum. Red line is a guide for eyes that has been extracted from fit by Kittel formula (Eq. 1.2) performed on a reduced set of frequencies. This procedure has been done by looking at Fig. 5.2b (dots are data, lines are the fits and red is for positive magnetic fields, black for negative), whose shape is supposed to be linear. There is a slight mismatch between the positive and negative fields that could be attributed to reminescence of the magnetization reversal when external magnetic field exceeds the coercive field as depicted Fig. 1.5a. Therefore, we reduced the frequency values on which perform the fit from 7.5 GHz to 12.5 GHz i.e. the part over which ΔH is linear in frequency, according to:

$$\Delta H = \Delta H_0 + f\frac{\alpha}{\gamma} \tag{5.2}$$

where ΔH_0 is the value at zero frequency f, α is the Gilbert damping parameter and γ is the is the gyromagnetic factor. The two profiles for positive and negative H are slightly different and this can be attributed again to hysteresis. In Fig. 5.2c a cut of the data taken at 10.5 GHz is shown as well as the fit according to Eq. 5.1. The shape is that of the derivative of a Lorentzian for both positive and negative magnetic fields, since absorbed power is always the same even if the direction of the magnetization is flipped. Therefore the spectrum is odd in magnetic field and two identical Lorentzian functions (even) are expected.

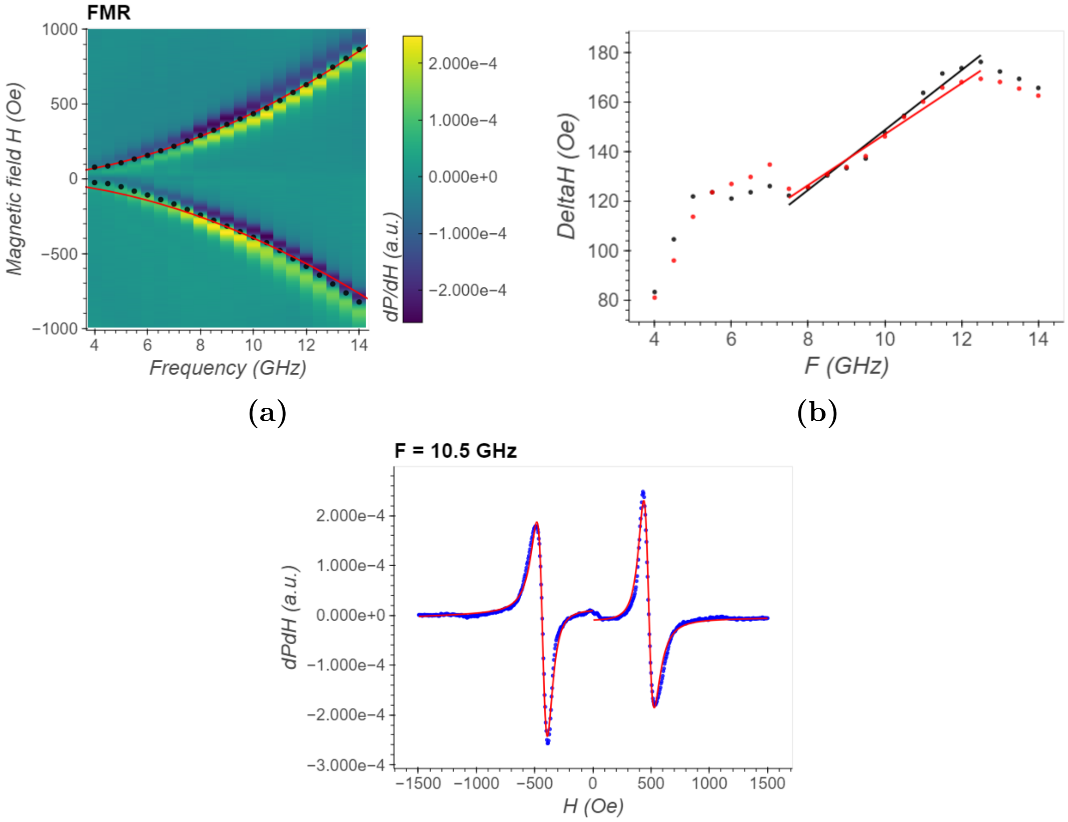

(a)

(b)

(c)

Figure 5.2: **(a)** FMR color-plot extracted from the data with lock-in technique. Black dots are the resonance frequencies extracted by fitting the data for each frequency as the derivative of a Lorentzian function; red line is a guide for the eyes and has been extracted by fitting the resonance frequencies according to Kittel formula (fit performed on a reduced set of data). **(b)** Half width at half maximum ΔH as a function of frequency. Dots are data, lines are the fits (performed in the linear part), while black represents data taken with the negative magnetic fields part of the spectrum and red with positive magnetic fields. **(c)** Cut performed at 10.5 GHz. Blue dots are data, red line the fits.

5.3 ISHE measurements

ISHE data are plotted too, in Fig. 5.3. The voltage across first three devices (with no Pd bar) is recorded (derivative with respect to magnetic field): in Fig. 5.3a similar color-plot as shown above for FMR is reported; even if the signal seems very weak in amplitude, it is still possible to see that the signal follows the same patter. Black dots represent fitted resonance frequencies, whose fit has been performed on a reduce set of data since the intensity of the signal was too weak and noisy to allow us to distinguish the expected shape for $\frac{dV}{dH}$ (according to Eq. 5.1). Red line is a guide for the eyes (again extracted from Kittel formula). As shown in the cut performed at 10.5 GHz (Fig. 5.3b), the shape is clear and corresponds to the derivative of Lorentzian. However, differently with respect to FMR power, the parity of the spectrum changes. By reversing the magnetization direction, the voltage change signs since the spin current does too. Then $\frac{dV}{dH}$ is even in H such that the voltage (Lorentzian) is odd.

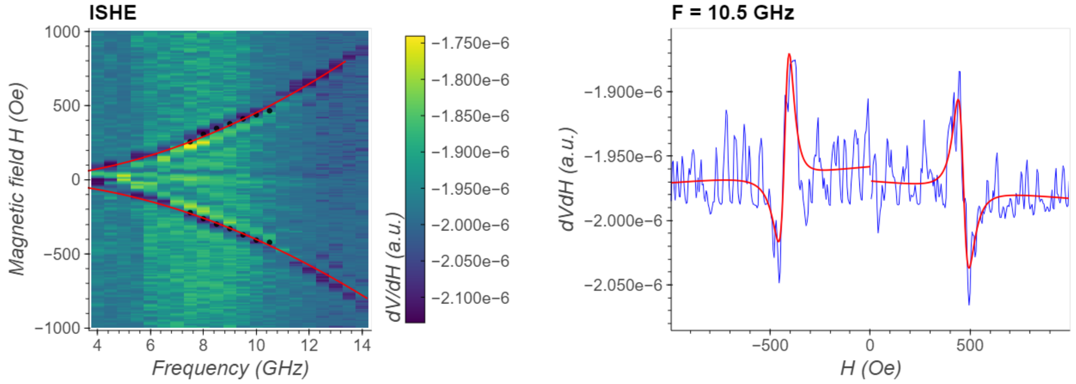

(a) **(b)**

Figure 5.3: (a) ISHE color-plot extracted from the data with lock-in technique. Black dots are the resonance frequencies extracted by fitting the data for each frequency as the derivative of a Lorentzian function; red line is a guide for the eyes and has been extracted by fitting the resonance frequencies according to Kittel formula (every ISHE has been fit performed on a reduced set of data). **(b)** Cut performed at 10.5 GHz. Blue dots are data, red line the fits.

These are very promising results since it is the very first time that in the team we manage to measure ISHE voltage directly on WSe_2 and it encourages us to keep on that.

In the end, fitting all the data with Kittel formula allows us to extract α and the saturation (effective) magnetization; it can be done for both positive and negative magnetic fields and for both FMR and ISHE (fit parameters reported in Table 5.1 and 5.2). The mean value for α is $\sim 3{\cdot}10^{-2}$ radian per second per oersted (rad s^{-1} Oe^{-1}) extracted from FMR, while for ISHE the value is lower ($\sim 10^{-3}$), while $4\pi M_{eff}$ is $\sim$ 30 kOe from both FMR and ISHE. In my device it is however hard to quantify the contribution from Co on WSe_2 and from Co not on top of it, since the deposited material was designed to cover the irregular shapes of the flakes underneath; moreover, the linewidth of the absorption is strongly reduced when Co is on top of it. In terms of magnetic anisotropy, the really thin Co layer leads to the 2D limit such that the magnetization prefers to be in plane; however, depending on the substrate on top of which Co is placed [26], another contribution (surface magnetic anisotropy) is included [27], thus making difficult to decouple the contribution of WSe2 as a substrate from the one where it is not present, so they both contribute to the effective magnetization.

	Negative magnetic fields	**Positive magnetic fields**
α (rad s^{-1} Oe^{-1})	$3.38 \cdot 10^{-2}$	$2.87 \cdot 10^{-2}$
$4\pi M_{eff}$ (kOe)	31.836	28.377
ΔH_0 (Oe)	27.959	44.435

Table 5.1: FMR fit parameters.

	Negative magnetic fields	**Positive magnetic fields**
α (rad s^{-1} Oe^{-1})	$5.8 \cdot 10^{-3}$	10^{-2}
$4\pi M_{eff}$ (kOe)	31.347	27.742
ΔH_0 (Oe)	67.035	61.101

Table 5.2: ISHE fit parameters.

Unfortunately, no DC resistance signal is recorded from the samples presenting palladium on top so no ISHE measurement can be run on them. Further investigation has to be put in order to understand which step should be improved to avoid the failing of the device, and then further effort has to be put to know how to achieve both efficient spin propagation along the 2D channel and spin to charge conversion for detection.

6. Conclusions and perspectives

This report outlines the problems, the background, and the scientific goals of the internship project. This experience offered to me a completely new experience in the field of experimental physics and spintronics. I had the possibility to discover an amazing field of research in which I did my best to get the most important concepts and ideas; moreover I had the opportunity and the pleasure to work with a composite team, whose members offered their knowledge in order to make me feel at ease and to make me perform the internship at best. Therefore I would like to thank my supervisors François Mallet and Clément Barraud for explaining me all the physical and technological concepts useful to build my device and to enrich my knowledge, and Karen Sobnath: I had the honor to work at her side and during her PhD she taught me everything she knows about the project and about the fabrication process. Beyond them I would like to thank the whole team for their precious help. I put lot of effort and I will do it in the future in understanding what improvements we can get from the device. Even if we did not manage to test all the configurations we planned, the data that were analyzed are very exciting and promising, paving the way towards new geometries of the device that will certainly be investigated in the future since I became totally independent in the fabrication protocol for this kind of device. Next steps will lead us to apply gate voltage on the 2D material (in order to tune the signal and observe what happens in presence of charge injection), to extract spin Hall angle for Co/WSe$_2$ interface, to apply transverse magnetic field and to probe spin propagation along WSe$_2$. I will have the opportunity to work again with the team during my career thanks to the PhD so I expect to ameliorate the fabrication steps and to get new exciting results.

A. Low-pass filter

This section is intended to briefly detail the characterization performed on the electrical (passive) low-pass filter used in the low-frequency and low-noise DC measurements described above.

The schematics of the filter is presented below:

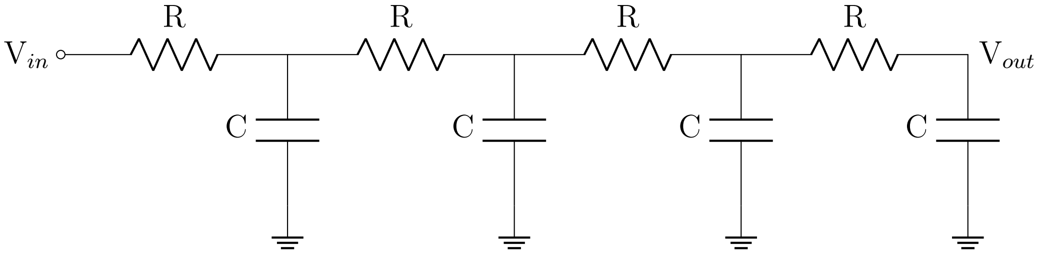

and can be used in two different configurations i.e. either with 1 pF or 100 pF capacitance. Then, according to the performed tests, the *Bode diagram*, both in terms of magnitude and phase, can be inspected and fitted according to the theoretical calculations for the transfer function V_{out}/V_{in}. By doing so it is possible to check if the values of the capacitance and of the resistance are correct and then see if parasitic elements are present, as well as if the forbidden band acts as predicted and if it attenuates by a sufficient amount of reduction the noise. As shown in the previous circuit, the resistance R is fixed at 10 MΩ, while the capacitance C can assume two different values: consequently, the response function will change. According to the theory, the transfer function H(jω) is:

$$H(j\omega) = \frac{1}{1 + 10jx - 15x^2 - 7jx^3 + x^4} \tag{A.1}$$

where j is the imaginary unit, x is ω/ω_c and ω_c is the cut-off frequency equal to *1/RC*. The corresponding Bode diagram is shown in Fig. A.1a and A.1b (blue and red curves). To complete the theoretical description of the filter, the measurements that have been performed on it have also additional components in series that attenuate further the signal, due to the oscilloscope and the probe, that can be schematized like:

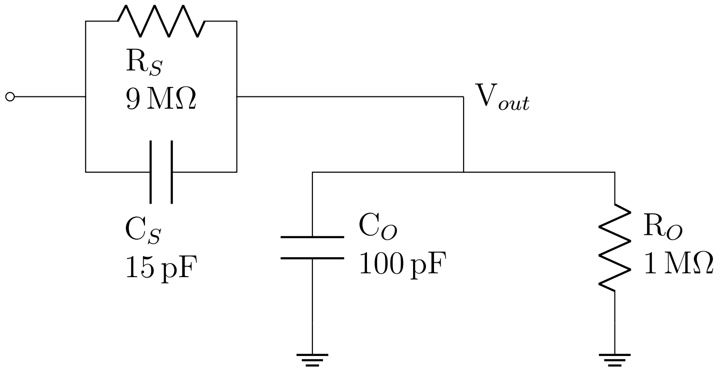

Its Bode diagram is shown in Fig. A.1a and A.1b (green and black curves). As visible in the figure, at low frequency the resulting attenuation is of -33 dB.

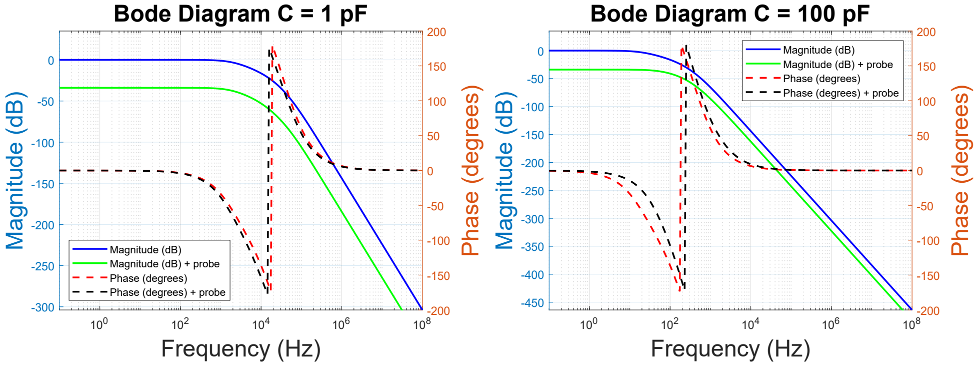

(a) **(b)**

Figure A.1: Bode diagrams: left vertical axis is magnitude in decibels (dB i.e. $20 \cdot \log_{10}(V_{out}/V_{in})$.) while right vertical axis is phase in degrees. Graphs with and without the compensation probe and the oscilloscope in series. The data are simulated thanks to *LTspice*.

Let us now see the actual measurements. As shown in Fig. A.2, the data were taken up to 1 kHz approximately, normalized to 1 (0 dB) at low frequency, and then fitted according to Eq. A.1; the fitting parameter was set to be the product RC that is ω_c^{-1}. In the first (left) case, the result was $2.79 \cdot 10^{-5}$, that is C = 2.79 pF, by setting R = 10 MΩ. In the second (right) case C = 37.25 pF, suggesting in both cases the presence of parasitic (capacitive) elements.

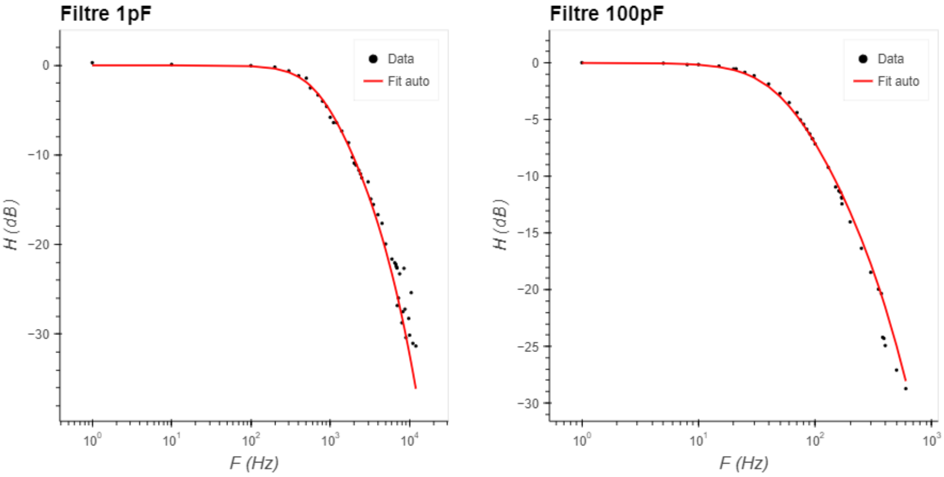

(a) **(b)**

Figure A.2: Data (black dots) from 1 pF and 100 pF capacitance filters and correspondent (red) fit to transfer function (Eq. A.1).

Despite the presence of parasitic elements, ultra-low-frequency (DC) measurements can still be performed due to a enough large band.

Bibliography

[1] M. N. Baibich, J. M. Broto, A. Fert, F. Nguyen Van Dau, F. Petroff, P. Etienne, G. Creuzet, A. Friederich, and J. Chazelas. «Giant Magnetoresistance of (001)Fe/(001)Cr Magnetic Superlattices». In: *Phys. Rev. Lett.* 61 (21 Nov. 1988), pp. 2472–2475. DOI: 10.1103/PhysRevLett.61.2472. URL: https://link.aps.org/doi/10.1103/PhysRevLett.61.2472 (cit. on p. 2).

[2] G. Binasch, P. Grünberg, F. Saurenbach, and W. Zinn. «Enhanced magnetoresistance in layered magnetic structures with antiferromagnetic interlayer exchange». In: *Phys. Rev. B* 39 (7 Mar. 1989), pp. 4828–4830. DOI: 10.1103/PhysRevB.39.4828. URL: https://link.aps.org/doi/10.1103/PhysRevB.39.4828 (cit. on p. 2).

[3] M. Julliere. «Tunneling between ferromagnetic films». In: *Physics Letters A* 54.3 (1975), pp. 225–226. ISSN: 0375-9601. URL: https://www.sciencedirect.com/science/article/pii/0375960175901747 (cit. on p. 2).

[4] Albert Fert. «Nobel Lecture: Origin, development, and future of spintronics». In: *Rev. Mod. Phys.* 80 (4 Dec. 2008), pp. 1517–1530. URL: https://link.aps.org/doi/10.1103/RevModPhys.80.1517 (cit. on p. 3).

[5] Yanping Liu, Cheng Zeng, Jiahong Zhong, Junnan Ding, Zhiming M. Wang, and Zongwen Liu. «Spintronics in Two-Dimensional Materials». In: *Nano-Micro Letters* 12.1 (Apr. 2020). ISSN: 2150-5551. URL: http://dx.doi.org/10.1007/s40820-020-00424-2 (cit. on p. 3).

[6] A. Avsar, H. Ochoa, F. Guinea, B. Özyilmaz, B. J. van Wees, and I. J. Vera-Marun. «Colloquium: Spintronics in graphene and other two-dimensional materials». In: *Rev. Mod. Phys.* 92 (2 June 2020), p. 021003. DOI: 10.1103/RevModPhys.92.021003. URL: https://link.aps.org/doi/10.1103/RevModPhys.92.021003 (cit. on p. 3).

[7] Ethan C. Ahn. «2D materials for spintronic devices». In: *npj 2D Materials and Applications* 4.1 (June 2020). ISSN: 2397-7132. DOI: 10.1038/s41699-020-0152-0. URL: http://dx.doi.org/10.1038/s41699-020-0152-0 (cit. on p. 3).

[8] A. K. Geim and I. V. Grigorieva. «Van der Waals heterostructures». In: *Nature* 499.7459 (July 2013), pp. 419–425. ISSN: 1476-4687. DOI: 10.1038/nature12385. URL: http://dx.doi.org/10.1038/nature12385 (cit. on p. 4).

[9] Matthew Yankowitz, Jiamin Xue, Daniel Cormode, Javier D. Sanchez-Yamagishi, K. Watanabe, T. Taniguchi, Pablo Jarillo-Herrero, Philippe Jacquod, and Brian J. LeRoy. «Emergence of superlattice Dirac points in graphene on hexagonal boron nitride». In: *Nature Physics* 8.5 (Mar. 2012), pp. 382–386. ISSN: 1745-2481. URL: http://dx.doi.org/10.1038/nphys2272 (cit. on p. 4).

[10] Rebeca Ribeiro-Palau, Changjian Zhang, Kenji Watanabe, Takashi Taniguchi, James Hone, and Cory R. Dean. «Twistable electronics with dynamically rotatable heterostructures». In: *Science* 361.6403 (2018), pp. 690–693. URL: https://www.science.org/doi/abs/10.1126/science.aat6981 (cit. on p. 4).

[11] S. Omar and B. J. van Wees. «Spin transport in high-mobility graphene on WS_2 substrate with electric-field tunable proximity spin-orbit interaction». In: *Phys. Rev. B* 97 (4 Jan. 2018), p. 045414. URL: `https://link.aps.org/doi/10.1103/PhysRevB.97.045414` (cit. on p. 4).

[12] Yaroslav Tserkovnyak, Arne Brataas, and Gerrit E. W. Bauer. «Spin pumping and magnetization dynamics in metallic multilayers». In: *Phys. Rev. B* 66 (22 Dec. 2002), p. 224403. URL: `https://link.aps.org/doi/10.1103/PhysRevB.66.224403` (cit. on p. 4).

[13] Anjan Soumyanarayanan, Nicolas Reyren, Fert Albert, and C. Panagopoulos. «Emergent Phenomena Induced by Spin-Orbit Coupling at Surfaces and Interfaces». In: *Nature* 539 (Nov. 2016), pp. 509–517. DOI: `10.1038/nature19820` (cit. on p. 5).

[14] David Indolese, Simon Zihlmann, Péter Makk, Christian Jünger, Kishan Thodkar, and Christian Schönenberger. «Wideband and On-Chip Excitation for Dynamical Spin Injection into Graphene». In: *Phys. Rev. Appl.* 10 (4 Oct. 2018), p. 044053. DOI: `10.1103/PhysRevApplied.10.044053`. URL: `https://link.aps.org/doi/10.1103/PhysRevApplied.10.044053` (cit. on p. 5).

[15] Richard Mattana, Nicolas Locatelli, and Vincent Cros. «Spintronics and Synchrotron Radiation». In: (2021). Ed. by Hervé Bulou, Loïc Joly, Jean-Michel Mariot, and Fabrice Scheurer, pp. 131–163 (cit. on p. 6).

[16] Paul Noel. «Dynamical spin injection and spin to charge current conversion in oxide-based Rashba interfaces and topological insulators». Theses. Université Grenoble Alpes, Nov. 2019. URL: `https://theses.hal.science/tel-02619764` (cit. on p. 9).

[17] M. I. D'yakonov and V. I. Perel'. «Possibility of Orienting Electron Spins with Current». In: *JETP Letters* 13 (11 1971), p. 657. URL: `http://jetpletters.ru/ps/0/article_24366.shtml` (cit. on p. 8).

[18] M.I. Dyakonov and V.I. Perel. «Current-induced spin orientation of electrons in semiconductors». In: *Physics Letters A* 35.6 (1971), pp. 459–460. ISSN: 0375-9601. URL: `https://www.sciencedirect.com/science/article/pii/0375960171901964` (cit. on p. 8).

[19] K. Ando and E. Saitoh. «Inverse spin-Hall effect in palladium at room temperature». In: *Journal of Applied Physics* 108.11 (Dec. 2010), p. 113925. URL: `https://doi.org/10.1063/1.3517131` (cit. on p. 11).

[20] X. D. Tao, Z. Feng, B. F. Miao, L. Sun, B. You, D. Wu, J. Du, W. Zhang, and H. F. Ding. «The spin Hall angle and spin diffusion length of Pd measured by spin pumping and microwave photoresistance». In: *Journal of Applied Physics* 115.17 (Jan. 2014), p. 17C504. ISSN: 0021-8979. URL: `https://doi.org/10.1063/1.4862215` (cit. on p. 11).

[21] K. Harii, K. Ando, K. Sasage, and E. Saitoh. «Detection of inverse spin-Hall effect in palladium». In: *physica status solidi c* 4.12 (2007), pp. 4437–4440. URL: `https://onlinelibrary.wiley.com/doi/abs/10.1002/pssc.200777281` (cit. on p. 11).

[22] Xinde Tao et al. «Self-consistent determination of spin Hall angle and spin diffusion length in Pt and Pd: The role of the interface spin loss». In: *Science Advances* 4.6 (2018), eaat1670. URL: `https://www.science.org/doi/abs/10.1126/sciadv.aat1670` (cit. on p. 11).

[23] K. S. Novoselov, A. K. Geim, S. V. Morozov, D. Jiang, Y. Zhang, S. V. Dubonos, I. V. Grigorieva, and A. A. Firsov. «Electric Field Effect in Atomically Thin Carbon Films». In: *Science* 306.5696 (2004), pp. 666–669. DOI: `10.1126/science.1102896`. URL: `https://www.science.org/doi/abs/10.1126/science.1102896` (cit. on p. 15).

[24] Filippo Pizzocchero, Lene Gammelgaard, Bjarke S. Jessen, José M. Caridad, Lei Wang, James Hone, Peter Bøggild, and Timothy J. Booth. «The hot pick-up technique for batch assembly of van der Waals heterostructures». In: *Nature Communications* 7.1 (June 2016). ISSN: 2041-1723. DOI: `10.1038/ncomms11894`. URL: `http://dx.doi.org/10.1038/ncomms11894` (cit. on pp. 16, 17).

[25] D. G. Purdie, N. M. Pugno, T. Taniguchi, K. Watanabe, A. C. Ferrari, and A. Lombardo. «Cleaning interfaces in layered materials heterostructures». In: *Nature Communications* 9.1 (Dec. 2018). ISSN: 2041-1723. DOI: `10.1038/s41467-018-07558-3`. URL: `http://dx.doi.org/10.1038/s41467-018-07558-3` (cit. on p. 16).

[26] Shugo Yoshii, Keisuke Kato, Ei Shigematsu, Ryo Ohshima, Yuichiro Ando, Koji Usami, and Masashi Shiraishi. «Significant suppression of two-magnon scattering in ultrathin Co by controlling the surface magnetic anisotropy at the Co/nonmagnet interfaces». In: *Phys. Rev. B* 106 (17 Nov. 2022), p. 174414. URL: `https://link.aps.org/doi/10.1103/PhysRevB.106.174414` (cit. on p. 27).

[27] A. K. Patra, S. Singh, B. Barin, Y. Lee, J.-H. Ahn, E. del Barco, E. R. Mucciolo, and B. Özyilmaz. «Dynamic spin injection into chemical vapor deposited graphene». In: *Applied Physics Letters* 101.16 (Oct. 2012). ISSN: 1077-3118. URL: `http://dx.doi.org/10.1063/1.4761932` (cit. on p. 27).